University of Alberta

LIGHT PROPAGATION AND PHOTOTHERMAL NONLINEARITY IN GRAPHENE-SI WAVEGUIDES

by

Cameron Steve Horvath

A thesis submitted to the Faculty of Graduate Studies and Research
in partial fulfillment of the requirements for the degree of

Master of Science
in
Photonics and Plasmas

Electrical and Computer Engineering

Fall 2013
Edmonton, Alberta

To the memory of my father,

Your encouragement of my passions early in life inspired me to follow the rewarding path I am on now.

Abstract

This thesis involves the study of light propagation and photothermal nonlinearity in graphene-silicon waveguides. Graphene, a two-dimensional monolayer of carbon atoms, is attracting a significant amount of interest due to its unique optical properties and its ability to be integrated with existing waveguiding materials such as silicon. Useful graphene photonic devices such as polarizers, modulators and couplers have been demonstrated in literature so far.

Photolithographic patterning techniques that allow for graphene patterning to occur on photonic devices before and after their on-chip realization were developed. Numerical simulations were performed that model the propagation loss and ohmic self-heating in graphene-silicon waveguides. A graphene-silicon waveguide was realized by transferring graphene onto a pre-existing silicon Fabry-Pérot waveguide resonator. The linear propagation loss and photothermal nonlinearity of the material system was investigated and compared to a bare silicon waveguide. An 8.8-fold enhancement in the effective thermal nonlinear index was observed.

Acknowledgements

First and foremost, I would like to offer my gratitude to my research supervisor, Prof. Vien Van. His unwavering support, constant guidance and advice over the years have not only made this thesis work possible, but have shaped me into a better individual. My labmates at the Nanophotonics Research Laboratory have been amazing to work with. Thanks to Daniel Bachman for providing silicon waveguides to work with and for our many discussions in the lab. My thanks also extends to Ashok Prabhu Masilamani, Alan Tsay, Siamak Abdollahi, Rice (Guangcan) Mi, Ken (Xiaoqin) Lei, Marcelo Wu and David Perron.

The fabrication part of my work would not have been possible without the training and assistance of the University of Alberta nanoFAB staff. Ken Bosnick and the other members of the Graphene Project at NINT also gave me the opportunity to participate in insightful discussions involving graphene synthesis, transfer and characterization. Thanks to Rob Indoe for providing the initial graphene samples that kickstarted the work.

Lastly, I would like to thank my family and friends for being very supportive of my academic pursuits. They saw how important the work was to me and always offered their blessings.

This research work was financially supported by the Natural Sciences and Engineering Research Council (NSERC), Alberta Innovates Technology Futures (AITF) and the University of Alberta.

Contents

List of Tables

List of Figures

List of Symbols

λ	Wavelength
ω	Frequency
T	Transmittance
R	Reflectance
δ	Round-trip phase delay
α	Attenuation coefficient
κ	Extinction coefficient
τ	Scattering lifetime
E_F	Fermi energy
v_F	Fermi velocity
μ	Chemical potential
k	Wavevector
K	Thermal conductivity
I	Intensity
$\vec{J}$	Current density
ϵ_0	Permittivity of free space
μ_0	Permeability of free space
ϵ_r	Relative permittivity
n_0	Linear refractive index
n_g	Group refractive index
n_2	Nonlinear refractive index
χ	Nonlinear susceptibility
$\vec{E}$	Electric field
$\vec{H}$	Magnetic field
$\vec{P}$	Polarization
$\vec{S}$	Poynting vector
A_{eff}	Effective modal area
Γ	Coupling loss
ρ	Charge density
β_{TPA}	TPA coefficient

List of Abbreviations

VoIP	Voice over Internet Protocol
CMOS	Complimentary metal-oxide-semiconductor
SOI	Silicon-on-oxide
EBL	Electron-beam lithography
RIE	Reactive ion etch
SPP	Surface plasmon polariton
TM	Transverse-magnetic
TE	Transverse-electric
PDE	Partial differential equation
PMMA	Polymethyl methacrylate
PML	Perfectly matched layer
CVD	Chemical vapour deposition
NINT	National Institute for Nanotechnology
SEM	Scanning electron microscope
EDFA	Erbium doped fiber amplifier
FSR	Free spectral range
TPA	Two-photon absorption
FCA	Free-carrier absorption
FCD	Free-carrier dispersion
T-O	Thermo-optic
sccm	Standard cubic centimetres per minute
CCD	Charge-coupled device
IR	Infrared
PD	Photodetector

Chapter 1

Introduction

The increased use of streaming video, voice over IP (VoIP), and social networking services is driving the effort to find more efficient ways of transferring and processing large volumes of data. Photonic devices are becoming a central focus in these developments as electronic devices begin to encounter size and bandwidth limitations. Electrical wires that once carried telephone conversations and data are now being replaced with low-loss fiber optical cables, which allow for more bandwidth and less latency over very long distances. At the circuit board level, the use of optical interconnects has been demonstrated in transferring data from chip-to-chip by industry leaders such as Intel [23]. Integral to the design of these photonic devices is the selection of the appropriate materials. This chapter will discuss the motivation behind developing photonic devices and introduce the basic building blocks of these devices.

1.1 Performance of electronics vs. photonics

One of the biggest limitations of electrical devices is the available bandwidth that conductors are capable of handling. As electrical signals of higher frequency are sent along conventional conductors, the resistance of the conductor increases due to the skin effect [41]. Optical waveguides are able to transit light signals with a very impressive amount of capacity, rendering copper wires inferior in long-distance communications applications. Techniques such as wavelength-division multiplexing (WDM) allows for many channels of communication to exist over a single waveguide [34].

Power consumption can also be an issue for both electronic and photonic devices. As electronics are reduced in physical size, their electrical resistance increases and large amounts of heat can be dissipated. Heatsinks and power management systems can reduce the burden that heat has on electronic components. However, light propagating in a dielectric waveguide dissipates very little heat. Heat dissipation in optical devices can also be relied on to perform some useful processes that rely on the thermo-optic effect. For example, heaters can be placed near optical microring resonators to tune their resonant wavelengths (by changing the refractive index of the microring) by adjusting the temperature [42]. The work described later in this thesis uses heat dissipated from the absorption of light in graphene to alter the refractive index of a waveguide and demonstrate enhanced thermal nonlinearity.

Another limitation to consider is that the size of electronic devices is limited by the nanofabrication methods that currently exist. An important benchmark used by engineers to describe the sizes of transistors is the gate length. These gate lengths have continued to decrease in size until recently [12], when it was found that further decreasing the physical size of transistors would further degrade their electrical properties. Photonic devices also have a minimum size limitation that is due to the diffraction limit of light. Efforts are being made to find ways of circumventing this limitation with the use of metamaterials [50] and plasmonic waveguides [17].

1.2 Silicon photonic waveguides

The building block of integrated photonic devices is the waveguide, a structure that is designed to guide light along a defined path using core and cladding materials. The confinement and loss of electromagnetic energy inside a waveguide depends heavily on the optical properties and dimensions of the materials being used. A widely used platform for photonic devices involves silicon as the core waveguiding material. Silicon is an indirect bandgap semiconductor with a bandgap energy larger than that of light used in telecommunications systems (wavelength of $\lambda \approx 1.3$ - 1.6 μm) [24]. Because of this, silicon is transparent at these wavelengths and light propagating in silicon experiences very little loss. Confinement of light in a waveguide is related to the index contrast between the core and cladding materials, and so silicon's refractive index of n = 3.4 ensures that light is well confined to the waveguide when lower index materials are used as the cladding material. In silicon-on-insulator (SOI) waveguides, air (n = 1) and a SiO_2 buffer layer (n = 1.45) are used as cladding materials. This high index contrast is important in keeping the bending loss in waveguides low [20] and reducing coupling between devices that are in close proximity to one another.

Because silicon is an inexpensive CMOS-compatible material [24], silicon photonics is of great interest to companies that already process silicon-based electronics in their nanofabrication foundries. Integration that occurs between photonic and electronic devices can be done using the same materials and processes. As well, the large nonlinear susceptibility of silicon [7] enables the development of all-optical devices.

1.2.1 Fabry-Pérot resonator

Optical resonators can be made from waveguides and are used in a number of applications including electric field enhancement, switching, and filtering applications. Waveguides can act as a resonator if the input and output ports are highly reflective and the propagation loss in the waveguide is kept low. Such structure is called the "Fabry-Pérot" resonator and is shown in Fig. 1.1. Light exiting through the output facet will partially reflect and travel back in the opposite direction. Reflected light will also partially reflect from the input facet, causing the light to return to the output facet and interfere with light travelling in the same direction. The power transmittance for this kind of resonator is described by the following expression [22]:

$$T = \frac{G(1-R)^2}{(1-RG)^2 + 4R\sin^2(\delta/2)} \tag{1.1}$$

The path-length phase difference δ is a function of the length of the resonator, the refractive index of the material and the wavelength for normal incidence:

$$\delta = \left(\frac{2\pi}{\lambda_0}\right) 2nl \tag{1.2}$$

The reflectance R of the waveguide facets and the propagation loss $G = e^{-2\alpha z}$ of the cavity determine the transmittance of the resonator. The optical path length determines whether light constructively or destructively interferes. The transmission from the waveguide will be less than unity for the case of partial destructive interference, and reach its maximum for the case of constructive interference. For the lossless ($G = 1$) case at resonance, the output transmittance is equal to the input transmittance. This structure is used later in this thesis to investigate thermal nonlinearity in a silicon-graphene waveguide.

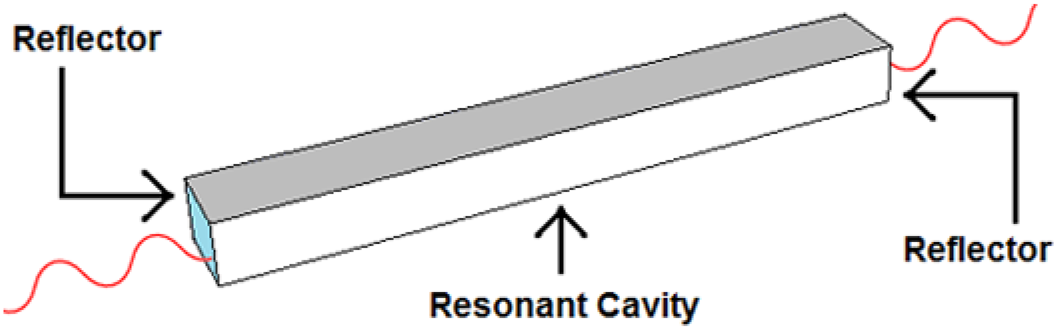

Figure 1.1: Fabry-Perot resonator consisting of two reflectors and a resonant cavity.

1.3 All-optical devices

Because of the bandwidth advantages of photonics components, as well as the fabrication difficulties associated with integrating photonic components with electronics, effort is being spent to develop “all-optical” photonic devices. These devices would be capable of performing complex signal processing operations without the use of electronics. However, in order for these devices to operate, multiple light signals would have to interact and influence one another, similar to how a transistor allows one electrical signal to control the flow of another. Light signals can be controlled optically using materials with strong nonlinear properties. The optical properties experienced by one light signal are dependent on the intensity of other light signals. Thermo-optic [40] and opto-mechanical effects [31] are some of the ways that all-optical devices have been demonstrated so far. Nonlinear optical phenomena will be described more in-depth in the next chapter.

1.4 Graphene as an optical material

Graphene is a two-dimensional material consisting of carbon atoms arranged in a hexagonal lattice. The 2010 Nobel Prize in Physics was awarded to André

Gaim and Konstantin Novoselov for their pioneering experiments involving graphene [39]. Graphene has interesting optical properties that arise from its linear electronic band structure. Among these properties are its high sheet absorption of light ($\approx 2.3\%$ absorption) [35], constant conductivity at optical frequencies [11, 25], and its ability to act as a nonlinear optical medium [19]. Graphene has recently been examined as a material for use in integrated photonic devices for a variety of applications. Of particular importance to the work done in this thesis are the thermal and electrical properties of graphene. The next chapter will give an in-depth overview of the various properties of graphene and give some examples of devices that have been reported in literature.

1.5 Thesis organization

This thesis is divided into six chapters, all of which focus on integrated photonic devices. Graphene photonics is the primary focus of the material. The layout is as follows:

- Chapter 2 gives an overview of the fundamental optical properties of graphene, and gives some examples of graphene devices studied in literature.

- Chapter 3 presents finite-difference numerical simulations that study the propagation characteristics of light and ohmic heating in a graphene-silicon waveguide.

- Chapter 4 gives a description of the synthesis and transfer of graphene in the production of graphene-based photonic devices. Work done on pre-device and post-device lithographic patterning is also presented.

- Chapter 5 describes the linear and nonlinear characterization of a graphene-silicon waveguide that demonstrates enhanced thermal nonlinearity and optical bistability.

- Chapter 6 provides a summary of the thesis and elaborates on future research directions for the work.

Chapter 2

Graphene Photonics

Graphene is attracting a significant amount of interest because of its unique and easily tunable optical properties. The optical properties of graphene are directly related to the way electrons behave in the material, and so graphene's optical material properties can be derived from its electrical conductivity. This chapter investigates the electrical properties of graphene, how the optical properties are related, and briefly examines the thermal properties of graphene that are relevant to the development of photonic devices. The chapter also showcases some graphene photonic devices that make use of these properties.

2.1 Electrical properties

2.1.1 Conductivity of single-layer graphene

Graphene's unique electrical properties arise from its linear electronic band structure ($E = \pm vp$, where $v \approx 10^6$ m/s), which resembles that of a photon [11]. This causes electrons in pure graphene to theoretically behave as if they have no mass. The electrical conductivity model of graphene is obtained from the band structure, and the derivation is described in detail in [11,25,32]. The expression for the conductivity of graphene contains two significant contributions: interband electron transitions and intraband absorption (Drude model response):

$$\sigma^{inter}(\omega) = \frac{e^2}{4\hbar}\left[\frac{1}{2} + \frac{1}{\pi}\arctan((\hbar\omega - 2\mu)/2kT - \frac{i}{2\pi}\ln\left[\frac{(\hbar\omega - 2\mu)^2 + (2kT)^2}{(\hbar\omega + 2\mu)^2 + (2kT)^2}\right]\right] \tag{2.1}$$

$$\sigma^{intra}(\omega) = \frac{ie^2|\mu|}{\pi\hbar^2(\omega + i\tau^{-1})} \tag{2.2}$$

$$\sigma^{total} = \sigma^{intra} + \sigma^{inter} \tag{2.3}$$

In the above expressions, k is the Boltzmann constant, T is the temperature, μ is the chemical potential, σ is the AC conductivity (in two-dimensional units, Ω^{-1}) and τ is the electron scattering lifetime. The scattering lifetime τ is dependent on the presence of impurities and electron-phonon scattering, which both impede the flow of electrons in the material [25]. The contribution due to impurities alone can be determined from the electron concentration n, electron mobility μ, and Fermi velocity v_F from the following expression:

$$\tau_{DC} = \frac{\mu\hbar\sqrt{n\pi}}{ev_F} \tag{2.4}$$

The contribution to the relaxation lifetime due to impurities is not frequency dependent. However, the contribution from electron-phonon scattering is, since it depends on the real part of the electrical conductivity and the frequency:

$$\tau_{el-ph}(\omega) = \frac{e^2 E_F}{\pi\hbar^2\omega^2}\frac{1}{\Re(\sigma(\omega))} \tag{2.5}$$

Jablan et al. estimated the value for τ_{DC} to be approximately 6.4×10^{-13} s, using $n = 3\times10^{13}$ cm^{-2} (corresponding to $E_F = 0.64$ eV), $\mu = 1\times10^4$ cm^2/V·s, and $v_F = 10^6$ m/s. For lower chemical potentials (Fermi levels), the electron population is lower and the relaxation lifetime is reduced. This acts to reduce the intraband conductivity, which plays a large part in the AC conductivity at low frequencies ($\hbar\omega < 2E_F$). The relaxation lifetime does not play a large role in the interband conductivity, which is dominant for frequencies in the infrared and visible range. The total relaxation lifetime can be found by combining the contributions from impurities and electron-phonon scattering:

$$\tau_{tot}^{-1} = \tau_{DC}^{-1} + \tau_{el-ph}^{-1} \tag{2.6}$$

The chemical potential μ (equivalent to the Fermi level) describes the maximum energy occupancy level of electrons in the material. For pure undoped graphene, there are only electrons in the valence band and μ is zero. The chemical potential can be adjusted through chemical doping or from applying a DC voltage between the graphene and an underlying substrate (electrostatic doping) [37]. This allows for the conductivity and consequently, the optical absorption, to be highly tunable. An electro-optic modulator using the principle of electrostatic doping was demonstrated by Liu et al, and is later described in this chapter.

The real and imaginary parts of the complex conductivity are plotted versus the photon energy in Fig. 2.1. It can be seen that for infrared and visible light ($\hbar\omega > 0.8$ eV), the conductivity approaches an asymptotic value of $e^2/4\hbar$, whereas the imaginary part stays at zero. For the case of zero chemical potential, interband transitions are the only contributing effect to the conductivity. The effect of increasing the chemical potential to 0.2 eV can be seen in Fig 2.2, where intraband transitions begin to have an effect. The real part of the conductivity becomes shifted to the right and a distinct transition between low and high conductivity can be seen at a photon energy of 2μ.

The relationship between the complex conductivity and chemical potential is plotted for a wavelength of 1.55 μm ($\hbar\omega = 0.8$ eV) in Fig. 2.3. When the chemical potential is above the interband transition energy of $\hbar\omega/2$ (≈ 0.4 eV), electrons occupy all of the possible states that photoexcited electrons can

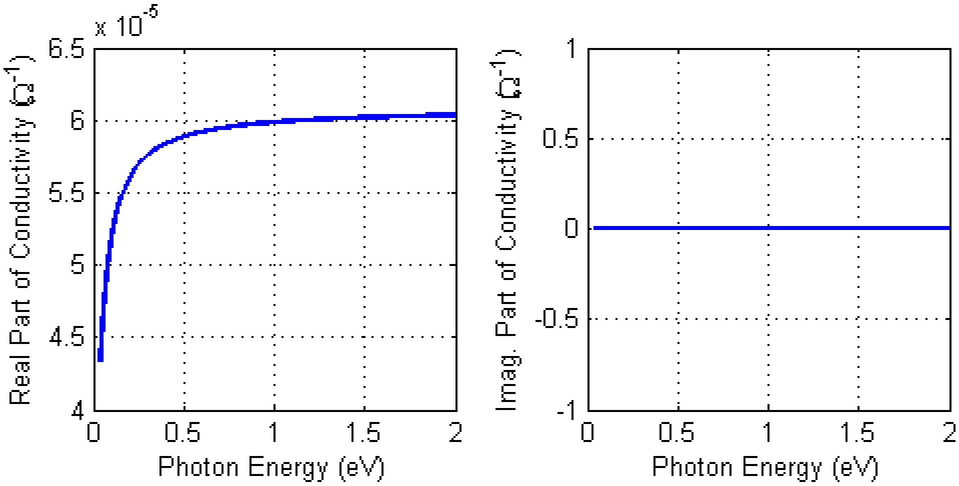

Figure 2.1: Complex conductivity of graphene at chemical potential of zero, scattering lifetime of 6×10^{-13} s and temperature of 295 K.

transition to, and the absorption of photons is decreased [35]. This transition can be modeled as a step function for absolute zero temperature, and becomes more gradual with increasing temperature.

2.1.2 Conductivity of multilayer graphene

Fabrication methods used to produce graphene often yield multiple layers, which will affect the electrical conductivity. A study on the conductivity of multilayer graphene was performed by Nakamura et al. in 2008. Their findings showed that the conductivity of graphene was given by the conductivity of a single layer multiplied by the number of layers N, if N is small [38]. This approach is used in [35,36] in the analysis of their devices which use multilayer graphene.

2.2 Optical properties

2.2.1 Dielectric constant and refractive index

The optical properties of solids depend heavily on the electronic properties. The AC conductivity and the relative dielectric constant of a 2D material are

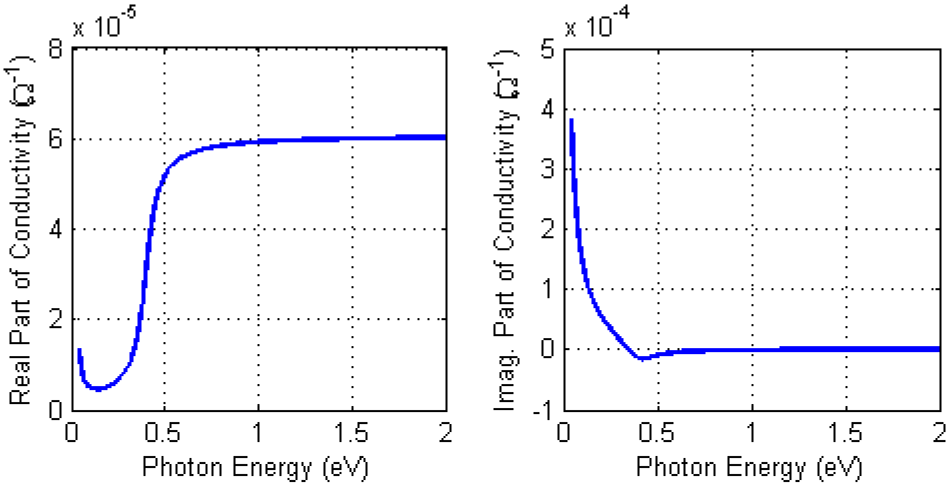

Figure 2.2: Complex conductivity of graphene at chemical potenial of 0.2 eV, scattering lifetime of 6×10^{-13} s and temperature of 295 K.

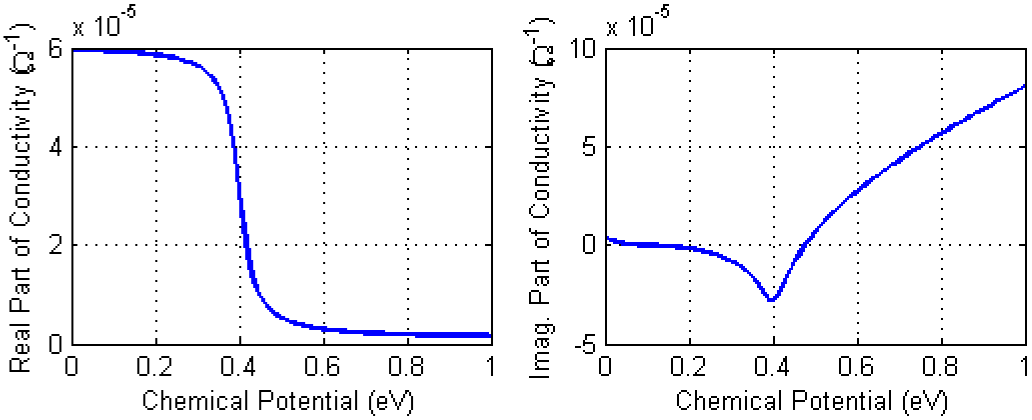

Figure 2.3: Complex conductivity of graphene at a wavelength of 1.55 μm, a scattering lifetime of 6×10^{-13} s and a temperature of 295 K.

related by the following expression [16]:

$$\epsilon_r(\omega) = 1 + \frac{i\sigma(\omega)}{\epsilon_0 \omega d} \tag{2.7}$$

In this equation, ϵ_0 is the permittivity of free space, $\sigma(\omega)$ is the frequency-dependent 2D conductivity of the material, d is the effective thickness of the layer and ω is the angular frequency of the light. It is assumed that the 2D conductivity of graphene can be estimated as a bulk 3D conductivity using $\sigma_{3D} = \sigma_{2D}/d$ [36]. Eqn. 2.7 is obtained from the Drude-Lorentz model, which describes how electrons behave in a material exposed to a time-varying electric field. The Drude part of the model describes the collisions that occur between electrons and positive ions in the crystal lattice. The Lorentz model treats the free electrons in the material as dipoles that oscillate as a result of being driven by the time-varying electric field.

The complex refractive index of a material describes both the phase change and attenuation of light in a material, and is related to the relative dielectric constant:

$$n_c = n + i\kappa = \sqrt{\epsilon_r} \tag{2.8}$$

The absorption coefficient α can be found from the extinction coefficient κ and free space wavelength λ_0 from:

$$\alpha = 2k\kappa = \frac{4\pi n\kappa}{\lambda_0} \tag{2.9}$$

The refractive index and absorption coefficient are plotted vs. chemical potential in Fig. 2.4 for wavelength 1.55 μm and scattering lifetime of 6×10^{-13} s. As the chemical potential is increased, the optical attenuation and refractive index both decrease. For a chemical potential of zero, graphene behaves as a lossy dielectric material with $n \approx 3.1$.

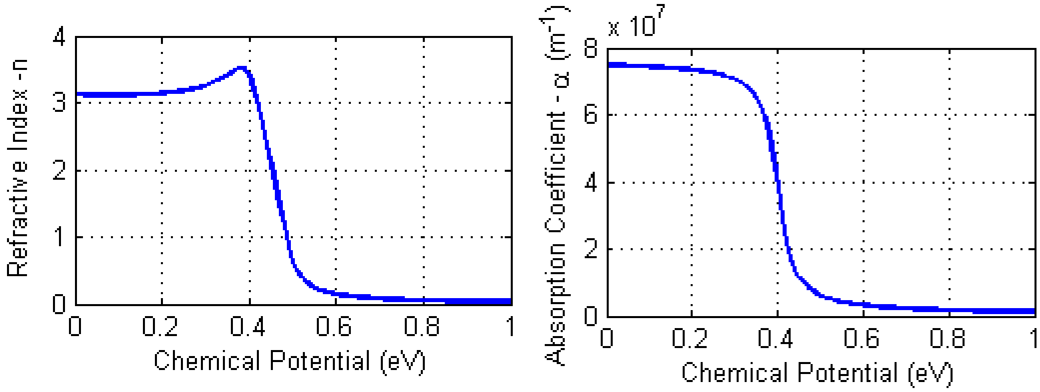

Figure 2.4: Refractive index and extinction coefficient of graphene vs. chemical potential for $\lambda = 1.55\mu$m, $\tau = 6 \times 10^{-13}$ s and thickness $d = 3.5\mathring{A}$.

2.2.2 Nonlinear susceptibility

Graphene also possesses a large third-order nonlinear susceptibility. Normally, the induced polarization of a linear material subject to an electric field is described by the relationship:

$$\vec{P}(t) = \epsilon_0 \chi \vec{E}(t) \tag{2.10}$$

where χ is the first-order susceptiblity. For nonlinear media such as graphene, the induced polarization can be expanded into higher order terms involving higher powers of the electric field [5]:

$$\vec{P}(t) = \epsilon_0 \left[\chi^{(1)} \vec{E}(t) + \chi^{(2)} \vec{E}^2(t) + \chi^{(3)} \vec{E}^3(t) + ... \right] \tag{2.11}$$

From $\chi^{(3)}$, the nonlinear refractive index (Kerr coefficient) can be calculated:

$$n_2 = \frac{3\chi^{(3)}}{8n_0} \tag{2.12}$$

In the above expression, n_0 is the linear index of refraction. The total index of refraction is related to the nonlinear refractive index and intensity of light by:

$$n = n_0 + n_2 I \tag{2.13}$$

In a graphene-silicon photonic crystal waveguide fabricated by Gu et al., n_2 was found to be 4.8×10^{-17} m^2/W [19]. In comparison, intrinsic silicon has an n_2 value of approximately 6×10^{-18} m^2/W [7]. This demonstrates that graphene has the potential to enhance the efficiency of $\chi^{(3)}$ processes such as four-wave mixing.

2.3 Thermal properties

Graphene is an excellent conductor of heat, with a thermal conductivity of approximately 5000 W/m K [3]. This is far larger than the value for metals such as copper (400 W/m K) and aluminum (250 W/m K). The thermal conductivity is an important parameter that determines the steady-state temperature of a material subject to a heat source.

Graphene also has a high amount of optical absorption. This ohmic loss manifests itself as a heat source in a waveguide system. The amount of heat power being generated in graphene can be estimated if the material conductivity and electric field in the material are known. The ohmic heat power generated in a material with conductivity σ can be calculated using [40]:

$$q = \frac{1}{2}\sigma|E|^2 \tag{2.14}$$

Heat generation in optical devices can have a detrimental effect on their performance, since a change in temperature can induce significant refractive index changes in a material with a large thermo-optic coefficient. Conversely, the generated heat can be used to induce useful changes in refractive index, such as in all-optical switches. The next chapter describes work that has been done in simulating thermal nonlinearity in a graphene-silicon waveguides.

2.4 Device examples

2.4.1 Electro-optic modulators

An electro-optic modulator based on the concept of electrostatic gating was demonstrated by Liu et al. in 2011 [35]. The device consists of graphene placed on top of a doped silicon waveguide designed to guide light at a wavelength of 1.53 μm. The waveguide is physically separated from the graphene using a 7-nm-thick Al_2O_3 buffer layer. The graphene layer is electrically connected to an Au-Pt electrode, whereas the silicon waveguide is in contact with the other electrode. Using an applied voltage across the two contact pads, the chemical potential (Fermi level) of the graphene is tuned such that the absorptive properties of graphene are also tuned.

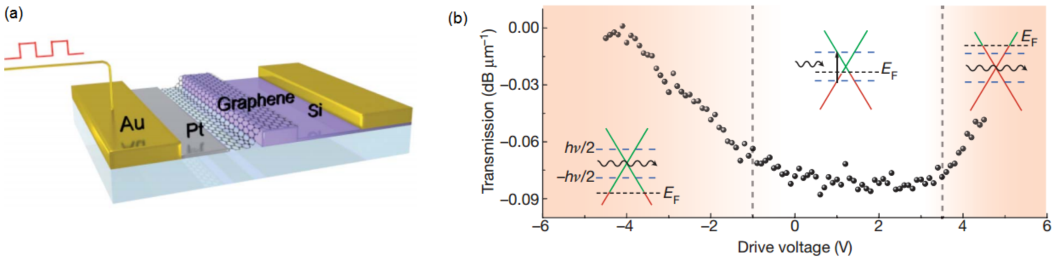

Figure 2.5: (a) Schematic of electro-optic modulator device from Liu et al. (b) Transmission of optical signal vs. drive voltage applied to the gold contact pads. There are three distinct regions of operation, which correspond to the shifting of the Fermi level. Reused from [35] with permission.

In Fig. 2.5, the transmission through the waveguide as a function of the applied voltage is plotted. For drive voltages lower than -1V, the Fermi level is below the interband transition energy of -$\hbar\omega/2$. This prevents any electrons from being available for interband transitions. For drive voltages near 0V, the Fermi level is near zero and graphene is highly absorptive since electrons are now available for interband transitions. For drive voltages higher than 3.8V, the Fermi level is large enough that electrons occupy all of the possible transition states that are in resonance with any photons, and so the photons are not absorbed. The minimum transmission is offset from zero-bias because the silicon waveguide is doped with boron (a p-type dopant), which shifts the Fermi level negatively. The modulation depth of the device, which is the ratio between maximum and minimum transmission in the device, was approximately 0.1 dB/μm.

2.4.2 Plasmonic waveguides

Graphene can be used to transport surface plasmon polaritons (SPPs) along it. SPPs are created when light couples to free electrons on the surface of a metal. When this occurs, light can be confined into a much smaller modal area and the effective SP wavelength of the light is much smaller than the free-space wavelength [25]. As mentioned in Chapter 1, plasmonics can be used to make photonic devices that circumvent the diffraction limit of light.

Plasmonic waveguides using graphene were demonstrated by Kim et al. in 2011 [29]. Graphene was physically transferred onto an cladding layer (n = 1.37) of thickness 20 μm. Using photolithography and reactive ion etching, the graphene was patterned into strips that were 5.7 mm-long. Another cladding layer of 20 μm was then placed on top. Light of wavelength 1.31 μm was coupled onto the graphene strip using a polarization-maintaining fiber. The coupling loss was measured to be 1 dB per facet for TM-polarization and the propagation loss for TM-polarization was 2.1 dB/mm. The corresponding propagation length is approximately 2.1 mm, which is considered to be long compared to conventional metal-dielectric material systems. Surface plasmons propagating along the top and bottom surfaces of the graphene form a well-confined guided mode. The output power was measured as a function of the polarization of the incoming light and it was found that when TE-polarized light is used, the insertion loss increases by 19 dB compared to TM-polarized light. This demonstrates that the performance of graphene plasmonic waveguides has a strong polarization dependency.

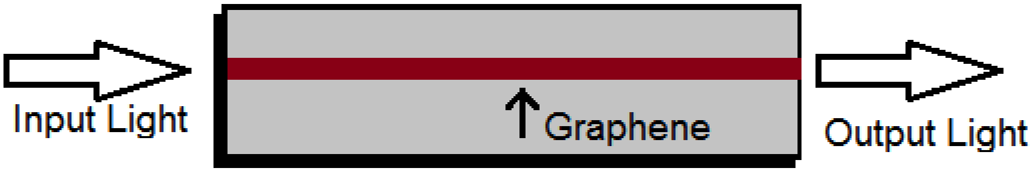

Figure 2.6: Schematic of graphene waveguides by Kim et al. Graphene strips of length 5.7 mm are patterned between a 20 μm-thick dielectric on both sides.

To demonstrate the practicality of the plasmonic waveguide, light pulses encoded with pseudorandom data were transmitted along the graphene strip at a rate of 2.5 Gbps. The bit-error-rate was measured to be 10^{-10} which demonstrates that virtually all of the data was readable at the output.

2.5 Summary

The electrical, optical and thermal properties of graphene were investigated in this chapter. The tunable chemical potential of graphene allows for the electrical conductivity (and by extension, the absorption) to be tuned by a variety of methods. This property has enabled electro-optic graphene devices to be experimentally demonstrated, such as the modulator device reported by Liu et al. The nonlinear optical properties of graphene have also been demonstrated in four-wave mixing experiments reported by Gu et al, and the work done on thermal nonlinearity described later in this thesis. Plasmonic waveguides, which allow for the subwavelength propagation of light, can also be realized with graphene as reported by Kim et al. These properties of graphene will be used in the simulations performed in the next chapter to investigate the nonlinear thermo-optic behaviour of graphene-silicon waveguides.

Chapter 3

Simulation of Graphene-Si Optical Devices

3.1 Helmholtz equation

Using the properties of graphene that were covered in the previous chapter, the optical performance of graphene devices can be modeled using analytical and numerical methods. The one-dimensional analytical expression for the optical slab mode will first be derived, which can be extended to 2D. We begin finding the electric field distribution in the graphene-silicon layers by solving the Helmholtz equation:

$$-\nabla \times \nabla \times \vec{E} + k_0^2 \vec{E} = j\omega\mu_0 \vec{J} \tag{3.1}$$

Since $-\nabla \times \nabla \times \vec{E} = \nabla^2 \vec{E} - \nabla \left(\nabla \cdot \vec{E}\right)$:

$$\nabla^2 \vec{E} + k_0^2 \vec{E} = j\omega\mu_0 \vec{J} + \nabla \left(\nabla \cdot \vec{E}\right) \tag{3.2}$$

The continuity of charge equation (in frequency domain) and Gauss's Law are:

$$\nabla \cdot \vec{J} = j\omega\rho \tag{3.3}$$

$$\nabla \cdot \vec{E} = \frac{\rho}{\epsilon_0} \tag{3.4}$$

If we combine Eqns. 3.3 and 3.4 by eliminating ρ, we get:

$$\nabla \cdot \vec{E} = \frac{-1}{j\omega\epsilon_0} \left(\nabla \cdot \vec{J}\right) \tag{3.5}$$

Substituting this into Eqn. 3.2 gives:

$$\nabla^2 \vec{E} + k_0^2 \vec{E} = j\omega\mu_0 \vec{J} + \frac{j}{\omega\epsilon_0} \nabla \left(\nabla \cdot \vec{J} \right) \tag{3.6}$$

3.1.1 One-dimensional treatment

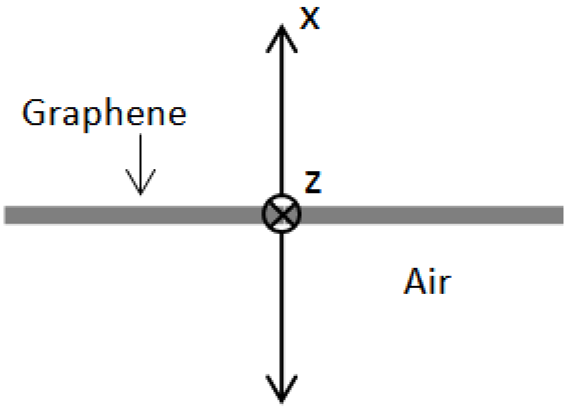

Figure 3.1: Schematic of one-dimensional graphene slab waveguide.

Fig. 3.1 depicts the one-dimensional graphene slab waveguide that will be investigated. When solving the Helmholtz equation in 1D, the direction of propagation of light is chosen to be in the ẑ direction and graphene is modeled as an infinite sheet with zero thickness in the x̂ direction. Transverse-magnetic (TM) polarization is assumed, where an electric field (but no magnetic field) is allowed to exist in the direction of propagation. The direction of current density is assumed to be in the direction of propagation, since the electrons are bound to the surface of the graphene (cannot move in the x̂ direction). In the 1D treatment, we can rewrite $\nabla \left(\nabla \cdot \vec{J} \right)$ as:

$$\nabla \left(\nabla \cdot \vec{J} \right) = (\nabla \otimes \nabla) \cdot \vec{J} = \begin{bmatrix} \frac{\partial^2}{\partial x^2} & \frac{\partial^2}{\partial x \partial z} \\ \frac{\partial^2}{\partial z \partial x} & \frac{\partial^2}{\partial z^2} \end{bmatrix} \cdot \begin{bmatrix} 0 \\ J_z \end{bmatrix} = \begin{bmatrix} 0 \\ \frac{\partial^2 J_z}{\partial z^2} \end{bmatrix} \tag{3.7}$$

Therefore:

$$\nabla^2 \begin{bmatrix} E_x \\ E_z \end{bmatrix} + k_0^2 \begin{bmatrix} E_x \\ E_z \end{bmatrix} = j\omega\mu_0 \begin{bmatrix} 0 \\ J_z \end{bmatrix} + \frac{j}{\omega\epsilon_0} \begin{bmatrix} 0 \\ \frac{\partial^2 J_z}{\partial z^2} \end{bmatrix} \tag{3.8}$$

Solving the equation in terms of E_z gives:

$$\nabla^2 E_z + k_0^2 E_z = j\omega\mu_0 J_z + \frac{j}{\omega\epsilon_0} \frac{\partial^2 J_z}{\partial z^2} \tag{3.9}$$

Expanding the Laplacian into its partial derivative form gives:

$$\frac{\partial^2 E_z}{\partial x^2} + \frac{\partial^2 E_z}{\partial z^2} + k_0^2 E_z = j\omega\mu_0 J_z + \frac{j}{\omega\epsilon_0}\frac{\partial^2 J_z}{\partial z^2} \tag{3.10}$$

In frequency domain, the spatial variation of E_z and J_z along the ẑ axis can be described by:

$$\frac{\partial^2 E_z}{\partial z^2} = (-j\beta)^2 E_z = -\beta^2 E_z \tag{3.11}$$

$$\frac{\partial^2 J_z}{\partial z^2} = (-j\beta)^2 J_z = -\beta^2 J_z \tag{3.12}$$

where β is the wavevector in the direction of propagation. Therefore, the Helmholtz equation reduces to:

$$\frac{\partial^2 E_z}{\partial x^2} + (k_0^2 - \beta^2)E_z = j\omega\mu_0 J_z - \frac{j\beta^2}{\omega\epsilon_0} J_z \tag{3.13}$$

In order for there to be an exponentially decaying solution to the PDE (describing a bound mode), $\beta^2 > k_0^2$. Therefore, let $k^2 = \beta^2 - k_0^2$:

$$\frac{\partial^2 E_z}{\partial x^2} - k^2 E_z = \left(j\omega\mu_0 - \frac{j\beta^2}{\omega\epsilon_0}\right) J_z \tag{3.14}$$

or alternatively...

$$\frac{\partial^2 E_z}{\partial x^2} + (jk)^2 E_z = \left(j\omega\mu_0 - \frac{j\beta^2}{\omega\epsilon_0}\right) J_z \tag{3.15}$$

To find the transverse propagation vector k, the boundary element method can be used. This method can also be used to solve the PDE in two-dimensions, but this requires expanding Eqn. 3.8 into three coupled equations and the use of dyadic Green's functions [21], which becomes very intensive to set up. The solution $E_z(x)$ is assumed to be in the following form for solving the inhomogeneous Helmholtz PDE [46]:

$$E_z(x) = \left(j\omega\mu_0 - \frac{j\beta^2}{\omega\epsilon_0}\right) \int_{-\infty}^{+\infty} G(x|x')J_z(x')dx' \tag{3.16}$$

$G(x|x')$ is the Green's function for the Helmholtz equation in 1D:

$$G(x|x') = \frac{j}{2k} e^{-jk_x|x-x'|} \tag{3.17}$$

Since the only area where there is non-zero current density is on the graphene sheet (at $x' = 0$):

$$E_z(x) = j\omega\mu_0 G(x|0)J_z(0) - \frac{j\beta^2}{\omega\epsilon_0}G(x|0)J_z(0) \tag{3.18}$$

Using the boundary condition that $E_z(0) = J_z(0)/\sigma$ and evaluating the Green's function at $x = 0$ and $k_x = jk$:

$$E_z(0) = \frac{J_z(0)}{\sigma} = j\omega\mu_0\frac{j}{2(jk)}J_z(0) - \frac{j\beta^2}{\omega\epsilon_0}\frac{j}{2(jk)}J_z(0) \tag{3.19}$$

Simplifying:

$$k = j\omega\mu_0\frac{\sigma}{2} - \frac{j\beta^2\sigma}{2\omega\epsilon_0} \tag{3.20}$$

$$k = \frac{j\omega^2\mu_0\epsilon_0\sigma - j\sigma\beta^2}{2\omega\epsilon_0} = \frac{\sigma}{2\omega\epsilon_0}(j\omega^2\mu_0\epsilon_0 - j\beta^2) = \frac{j\sigma}{2\omega\epsilon_0}(k_0^2 - \beta^2) = \frac{-j\sigma}{2\omega\epsilon_0}k^2 \tag{3.21}$$

Therefore:

$$k = \frac{2j\omega\epsilon_0}{\sigma} \tag{3.22}$$

This result matches the wavevector for the TM surface mode described in [25]. k is an imaginary number (assuming the real part of σ dominates the imaginary part), which indicates that the electric field profile is exponentially decaying in the x̂ direction rather than oscillating to infinity. However, for this bound mode to exist, the dielectric constant of the graphene layer must be negative to satisfy the condition for surface plasmon polariton propagation [26]. This only occurs for photon energies in the terahertz frequency range (or lower energy). In the infrared/visible regime which is the regime we are working in, graphene acts as a lossy dielectric with a positive dielectric constant. Therefore, a thick enough high-dielectric layer (such as silicon) needs to be present for a photonic mode to be allowed to propagate. Since this makes the geometry more complex, the analysis was moved to using a numerical approach instead.

3.2 Numerical methods

While one-dimensional approach can present a simple analytical expression to use, it is easier to calculate the propagation constant for optical modes in complex two-dimensional structures using numerical methods. The boundary element method treats the graphene layer as a true infinitesmally-thin boundary, but the problem in two-dimensions is difficult to set up. As mentioned in the previous chapter, an effective 3D conductivity of graphene can be estimated by dividing the 2D conductivity by an effective thickness Δ. If this approximation is used, other numerical methods such as the finite difference or finite element method can be used to model graphene devices by treating the graphene as a layer with a 3D conductivity and effective thickness.

3.2.1 Finite element method

Numerical methods solve PDEs by taking the computational domain and discretizing it into a set of elements. Many discretization methods exist, but choosing one that allows smaller features to be computed properly is important. If step sizes are chosen to be too large, features smaller than the step size will not be approximated accurately. This is important in numerical simulations involving graphene, since the effective thickness of the graphene layer is much smaller than the thickness of the other materials present in the simulation. The finite element method allows for the computational domain to be discretized using a mesh that can be dynamically scaled in size depending on the feature sizes being simulated. Areas of the computational domain that lack smaller features can use a less dense mesh to ease the computational burden.

The simulations performed in this thesis have been done using commercial software (COMSOL), although the finite element method can be implemented manually in MATLAB or other programming environments. COMSOL provides much flexibility in creating custom meshes for specific structures, and allows the user to perform multiphysics simulations that link various types of simulations (such as electromagnetic, thermal, and mechanical) together.

3.3 Simulation of thermo-optic effect

3.3.1 Electromagnetic problem

Using the finite element method, the electric field distribution of light propagating in a graphene-silicon waveguide will be obtaned for TE and TM polarization. Afterward, the graphene strip and silicon waveguide will be modeled as heat sources and the temperature increase of the waveguide will be obtained for a given optical power. This temperature increase will then be used to determine the refractive index change in the silicon waveguide using the thermo-optic effect and demonstrate that the thermal nonlinearity in the waveguide is expected to increase with the addition of the graphene layer.

To begin, the layers listed in Table 3.1 are set up in the COMSOL electromagnetic simulation. The layers represent a 2 μm-wide waveguide structure patterned on a silicon-on-insulator substrate, with a polymethyl-methacrylate (PMMA) layer available for mechanical support of the graphene. This description of the fabrication and chacterization of the device is in the next chapter. To approximate an infinite region around the waveguide, the dimensions of the cladding layers (air, SiO_2 and PMMA) are made large enough to isolate the optical mode from the edge of the domain. The computational domain is set to have perfect electric conducting boundaries ($\hat{n}\times\vec{E} = 0$), but more rigorous methods such as using a perfectly matched layer (PML) could also be used.

Fig 3.2 shows a schematic of the proposed simulation scheme.

Table 3.1: Waveguide Material Properties

	Material Thickness (nm)	**Refractive Index**	**Electrical Conductivity ($\Omega^{-1} \cdot \mathrm{m}^{-1}$))**	**Thermal Conductivity (W/(m·K))**
Si	340	3.47	2.3×10^{-1}	149
SiO_2	1000	1.52	—	1.9
Graphene	0.35	3.00	5.0×10^{3}	5000 [3]
PMMA	1000	1.47	—	0.25
Air	340 (beside Si)	1.00	—	0.023

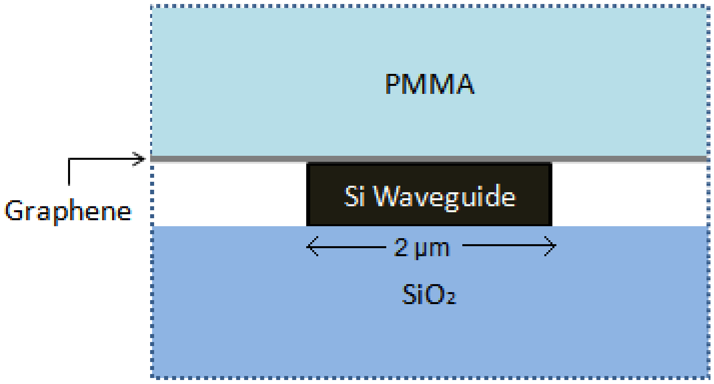

Figure 3.2: Schematic of the computational domain for the thermo-optic simulation of a graphene-Si waveguide.

Starting with the Helmholtz equation in Eqn. 3.1 in a medium with $k^2 = \epsilon_r k_0^2$ and using the relation $\vec{J} = \sigma\vec{E}$, one can obtain the form of the equation that COMSOL uses for its electromagnetic simulation:

$$\nabla \times \nabla \times \vec{E} - \left(\epsilon_r - \frac{j\sigma}{\omega\epsilon_0}\right) k_0^2 \vec{E} = 0 \tag{3.23}$$

For the graphene layer, σ is the real part of the effective 3D conductivity and ϵ_r can be found from the imaginary part of the conductivity using Eqn. 2.7.

The conductivity of $5.0 \times 10^3\ \Omega^{-1}m^{-1}$ for graphene for this simulation was chosen to be lower than the theoretical value, since the observed propagation loss (in the Chapter 5 experiments using the NINT graphene) was much lower than the expected propagation loss using the theoretical value. This can be due to the quality of graphene, the presence of dopants, or that the waveguide was not uniformly covered with graphene. Measured sheet resistance of graphene can often vary significantly from the theoretically expected values for these reasons [27]. The conductivity of graphene in this simulation was chosen to give a propagation loss of 19.3 dB/cm for TM polarization, which is the experimentally observed attenuation.

For the purely dielectric layers, the PDE reduces down to $\epsilon_r = n^2$ and $\sigma = 0$. A conductivity is calculated for silicon (based on an estimated material loss of 1 dB/cm [18]), so that heating in the silicon can be modeled, although its equivalent conductivity is much lower than that of graphene and is calculated using the following expression [40]:

$$\sigma = \alpha n \sqrt{\epsilon_0/\mu_0} \tag{3.24}$$

When the PDE is solved for light of wavelength $\lambda = 1.55\ \mu$m, many solutions for the propagation constant are found. These represent the eigenvalues of the various optical modes that are allowed to propagate in the waveguide. When searching for which solutions to use in the thermal analysis, the search is focused on the fundamental TE and TM modes. It is assumed that the the power propagating through our device is solely concentrated in the fundamental modes, and that the higher order modes are either much more lossy or not easily excited by the fiber butt-coupling scheme used in measuring these devices.

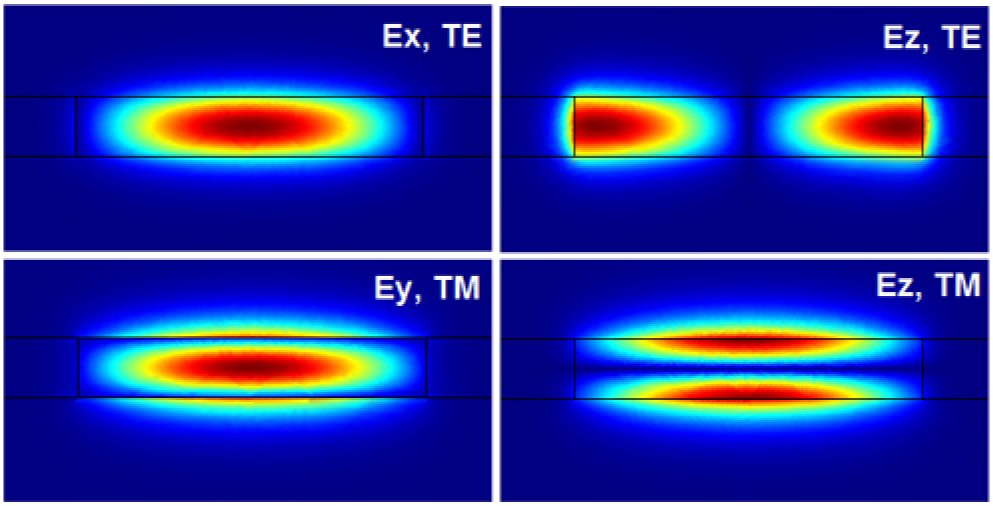

Figure 3.3: Simulated electric field distributions (in arbitrary units) in graphene-silicon waveguide for TE and TM-polarized light.

Fig. 3.3 shows the dominant electric field components that make up the fundamental TE and TM optical modes. The E_y field for TE and the E_x field for TM-polarization are much smaller in magnitude than the other fields and are not shown. The effective index and the propagation loss (calculated from the imaginary part of the wavevector from each mode) are given in Table 3.2.

Table 3.2: Electromagnetic Simulation Results

	Effective Index	**Propagation Loss (dB/cm)**
Graphene (TE)	3.09	9.5
Graphene (TM)	2.78	19.3
Bare Si (TM)	2.78	1.01

The electric field strength given by the COMSOL simulation is not normalized properly, and so the electric field must be normalized using the optical power in the waveguide for the thermal analysis to be properly done. The Poynting vector $\vec{S}$ describes the energy flux density (in units of W/m^2), which is the rate of energy transfer per unit area. The total energy transfer, or optical power, can be found by integrating the time-averaged Poynting vector over the 2D cross-section of the waveguide:

$$P_{tot} = \int_S \langle \vec{S} \rangle dy\, dx = \int_S \langle \vec{E} \times \vec{H} \rangle \, dy\, dx \tag{3.25}$$

Since the electric and magnetic fields are not normalized in the simulation, the true fields can be found by calculating a normalization constant m and applying it to each unnormalized field component (given by the subscript 0). To find m, the integrated Poynting vector is calculated by COMSOL using the unnormalized fields, and the result multiplied by a factor of m^2 will give the total optical power:

$$P_{tot} = m^2 \int_S \langle \vec{S_0} \rangle dy\, dx \tag{3.26}$$

$$m = \sqrt{\frac{P_{tot}}{\int_S \langle \vec{S_0} \rangle dy\, dx}} \tag{3.27}$$

Once m is determined, each unnormalized electric field component in the simulation can simply be multiplied by m to yield the absolute electric field in V/m:

$$E_x = mE_{x0} \qquad E_y = mE_{y0} \qquad E_z = mE_{z0} \tag{3.28}$$

The code implementation of this normalization scheme can be found in Appendix A. Calculating the absolute electric field strength is necessary to calculate the heat dissipation in the next section.

3.3.2 Thermal problem

The next step in determining the thermo-optic refractive index shift in the waveguide is to model the temperature distribution while the optical signal is propagating. As light is propagating in the waveguide, some of the light is absorbed in the graphene layer and in the silicon waveguide core. As shown in Eqn. 2.14, the amount of heat power produced from this absorption is proportional to the electrical conductivity of the material and the electric field strength. The relationship between the heat power q (in W/m^3), thermal conductivity K (in W/m·K) and the temperature T (in K) is related by the heat equation:

$$-\nabla \cdot (K\nabla T) = q \tag{3.29}$$

The thermal conductivity describes how easily the heat spreads in a material. While heat is allowed to spread through the silicon core and graphene layer very easily, it cannot spread through the SiO_2, PMMA, or into the ambient air as effectively because of their low thermal conductivities. This indicates that the generated heat will cause the temperature to be fairly constant in the waveguide, but taper off in the cladding materials. The boundary condition on the bottom of the SiO_2 layer is approximated to be at a constant temperature of $T = 295$ K. When being measured, the chip is in physical contact with an aluminum stage that is at room temperature. The remaining boundaries are set to be thermally insulating ($(\mathrm{K}\nabla \mathrm{T})\cdot\hat{\mathrm{n}} = 0$).

We neglect current flow along the y (out-of-plane) direction of the graphene layer, and so it is assumed that the E_y electric field does not contribute to ohmic heating and that only the E_x and E_z electric fields can contribute. All three electric field components contribute towards heating in the silicon core. Fig. 3.4 shows the steady-state temperature distribution in the waveguide for TE and TM-polarized light. The electric fields were normalized to 5 mW of optical power using Eqn. 3.27 and 3.28.

It can be seen that the TM polarization in graphene gives rise to the largest temperature rise in the waveguide core, with the TE-polarization giving approximately half of the temperature increase. Having no graphene present gives the least amount of heating.

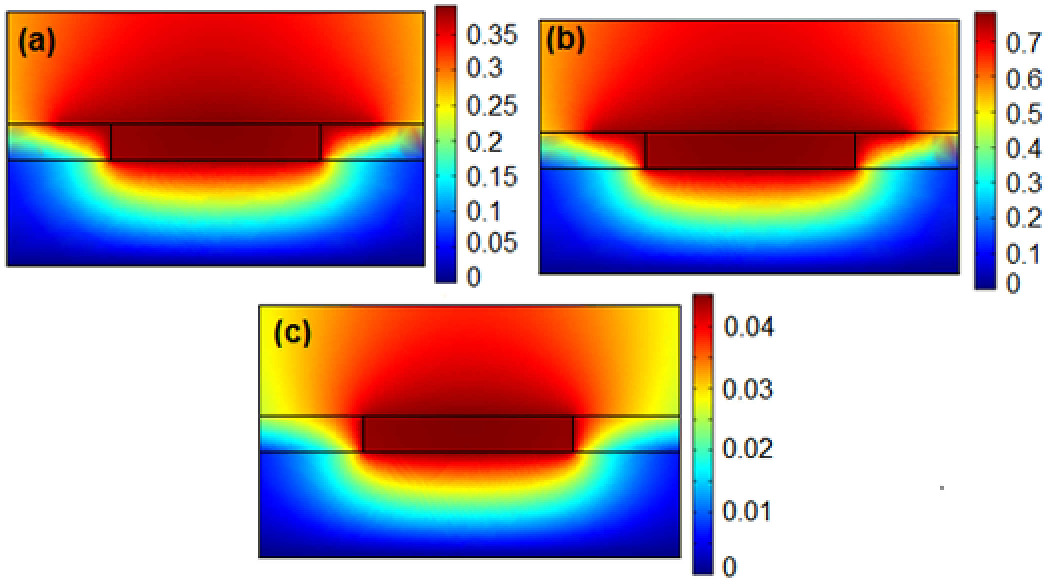

Figure 3.4: Simulated peak temperature distributions (relative to 295K) at 5 mW optical power for (a) TE, (b) TM, and (c) TM polarization without graphene.

3.4 Estimation of thermal nonlinear index

In Eqn. 2.13, it was shown that the index of refraction of a material can be represented by the linear index n_0 plus a nonlinear contribution that depends on the intensity of light and nonlinear refractive index n_2. Using the peak temperature rise from the simulation and thermo-optic coefficient of the silicon waveguide core, the nonlinear index due to thermal effects can be estimated. The thermal nonlinear index n_2 and the thermo-optic coefficient dn/dT are related by:

$$\Delta n = n_2 I = \left(\frac{dn}{dT}\right) \Delta T \tag{3.30}$$

The cross-sectional intensity I is a measure of the optical power per unit area, and can be calculated from the total optical power and the effective modal area from the electromagnetic simulation:

$$I_{avg} = \frac{P_{tot}}{A_{eff}} \tag{3.31}$$

The effective modal area is calculated from the weighted integration of the intensity (or electric field magnitude) over the entire computational domain [30]:

$$A_{eff} = \frac{\left(\int I\,dA\right)^2}{\int I^2\,dA} = \frac{\left(\int |\vec{E}|^2\,dA\right)^2}{\int |\vec{E}|^4\,dA} \tag{3.32}$$

The effective modal areas for the TE and TM modes were calculated to be 0.490 μm^2 and 0.760 μm^2 respectively. In the waveguide measured in Chapter 5, the light first propagates through a bare silicon region (L_{Si} = 0.4 mm) and then propagates through the region with graphene (L_G = 2.5 mm). There is another region of waveguide after this that has no graphene/PMMA layer, but the intensity is attenuated so much by the graphene region that this bare Si area contributes a negligible amount to the temperature rise. Using the temperature, the intensity in the waveguide (calculated from the power and effective modal area) and the thermo-optic coefficient of silicon (dn/dT = 1.84 × 10^{-4} K^{-1}), the nonlinear index of the waveguide is estimated for each case and is shown in Table 3.3 along with the temperature rises. Since the thermal conductivity of silicon is relatively high, the temperature across the entire waveguide core is assumed to be constant.

Table 3.3: Thermal Simulation Results

	Temperature Change (ΔT)	**Effective Nonlinear Index ($n_{2,eff}$)**
Graphene (TE)	0.39 K	7.06 × 10^{-11} cm^2/W
Graphene (TM)	0.74 K	2.07 × 10^{-10} cm^2/W
Bare Si (TM)	0.045 K	1.26 × 10^{-11} cm^2/W

3.5 Effect of PMMA

PMMA is often used as a mechanical support for CVD-grown graphene, since it is a material that is easily spun onto metal foils that have graphene grown on them. Although PMMA can act as a transparent cladding for waveguides operating at $\lambda = 1.55$ μm, its own thermal and optical properties can alter the performance of the waveguide slightly. The thermo-optic coefficient of PMMA has a value of -1.2 $\times$ 10^{-4} K^{-1} [8], which is of opposite sign to that of silicon. Combining materials with opposing thermo-optic coefficients is a technique used in athermal waveguides to mitigate the thermo-optic effect [43]. In this case, because the electric field strength in the PMMA cladding layer is low compared to the strength inside the waveguide core, the change in the effective index of the TE and TM mode is dominated by changes in the refractive index of silicon. However, it is expected that the enhancement would improve with the removal of the PMMA layer, since the remaining materials would all have a positive thermo-optic coefficient.

PMMA also has a thermal conductivity that is much greater than that of air. This creates an alternate route for heat to escape from the graphene layer, instead of heating the silicon waveguide core. Fig. 3.5 shows the temperature distribution in the waveguide for TM-polarized light with and without the PMMA cladding layer. The temperature in the core is seen to increase with the removal of PMMA from 0.74 K to 0.87 K. This will cause the n_2 value to be larger if PMMA is removed.

3.6 Limitations of simulation

The finite element method discretizes the computational domain using a mesh comprised of triangular elements that vary in density according to the structure's dimensions. Because of this, the thin layer of graphene must be represented using a large number of these elements. However, constraints in computational power prevent too many elements from being used in this simulation. A more accurate representation of the properties of graphene would occur if

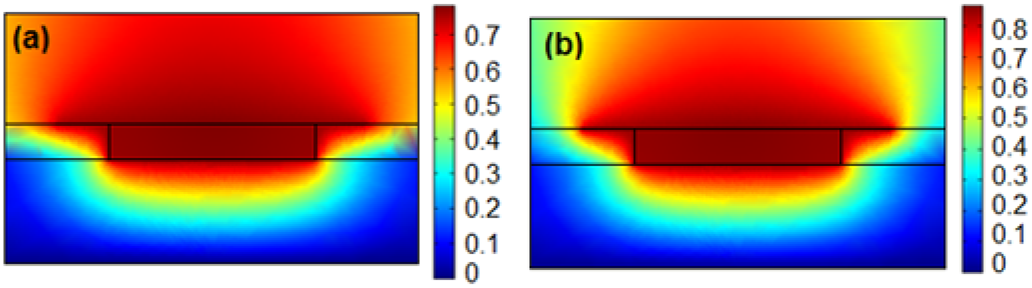

Figure 3.5: Simulated temperature distributions (relative to 295K) at 5 mW optical power for TM-polarized light (a) with PMMA and (b) without PMMA cladding layer.

more elements are used to represent the graphene layer. As well, graphene is modeled as a material with an isotropic 3D electrical conductivity. In reality, the in-plane conductivity of the graphene sheet is far greater than the perpendicular conductivity of bilayer graphene, which has been shown theoretically to be low everywhere except for near the interband transition energy [44]. Because of this, the electric field component E_y that causes electrons to move perpendicular to the graphene sheet is ignored when calculating the ohmic heating in graphene for the thermal simulation. Introducing an anisotropic conductivity into the simulation could better represent the ohmic self-heating observed in graphene waveguides.

Another assumption made in the simulation is that the 340 nm-thick silicon substrate that is in contact with the aluminum stage is represented as a constant temperature boundary condition. Including the entire substrate thickness in the simulation would require significantly more computational effort. Instead, it is assumed that any heat that is conducted through the oxide insulation layer will come into contact with silicon that is regulated at room temperature by the aluminum stage.

3.7 Summary

In this chapter, a simulation of a graphene-silicon waveguide was performed to investigate the effects of ohmic self-heating on the waveguide's optical properties. The simulation was done using the finite element method by approximating the graphene layer as a bulk medium with an isotropic conductivity and effective thickness. The result of the simulation is that ohmic self-heating in the graphene-silicon waveguide induces a refractive index shift that is related to the amount of power propagating in the waveguide. The dissipation of optical power in the graphene layer manifests itself as heat that causes the temperature of the silicon core to increase. This will slightly increase the index of refraction of the silicon waveguide core. The effect of having a PMMA support layer was briefly discussed, and it was found that further enhancement could be observed if the PMMA layer were removed.

The next chapter will give an overview into the synthesis methods that are currently used to produce graphene, and will outline the fabrication work done to transfer graphene onto substrates and pattern graphene using photolithography and O_2 etching.

Chapter 4

Graphene-Silicon Device Fabrication

4.1 Synthesis methods

To enable the development of graphene microelectronic and integrated photonic devices, much research is being done to reliably synthesize graphene on a large scale. One of the earliest methods of synthesizing graphene was through the mechanical exfoliation of bulk graphite by Novoselov et al. in 2004 [39]. Since then, methods such as chemical vapour deposition (CVD) and annealing of silicon carbide have been developed that allow for more reliable mass fabrication. Unlike mechanical exfoliation, these methods also provide more control over the orientation of the graphene film, which is important in electronics fabrication. [2].

With the CVD method, a metallic foil (usually copper or nickel) is placed in a chamber that is heated to approximately 900^{o}C in the presence of hydrogen and argon gas at atmospheric pressure. Methane, the source of carbon for the graphene layer, is fed into the chamber for 10 to 20 minutes and the carbon is absorbed into the metallic foil. The foil is then allowed to cool, causing the carbon to precipitate to the surface of the foil and form a graphene layer. Many of the process parameters such as temperature, rate of cooling, type of metal, and gas flow rates are controllable and influence quality and number of layers of graphene that form on the foil [6]. The graphene used in this thesis work is synthesized using CVD. The graphene-silicon waveguides fabricated in this work was done with graphene synthesized by the cleanroom staff at the National Institute for Nanotechnology (NINT) and at ACS Material. Using these samples, the work on photolithographic patterning was done in the U of A nanoFAB.

4.2 Graphene transfer process

The transfer of graphene from the metallic foil can be done either using a wet or dry method. However, the metal must first be removed and so the graphene needs to have a mechanical support layer (usually a polymer) placed on it until it is transferred onto the target substrate. Both sources of graphene for this thesis work use copper foil for graphene synthesis, and so the removal was done using an ammonium persulfate wet etchant before the samples were delivered.

The graphene provided by ACS Material and NINT both have a PMMA layer pre-spun on the samples. However, the graphene from ACS Material comes with a very thin layer of PMMA and so the dry transfer process will cause the graphene/PMMA sample to buckle during transport. In this case, the graphene can be transferred to a substrate using a water bath. The sample is introduced to the water bath, and is allowed to float freely. Using tweezers, the substrate is maneuvered in the water bath such that the floating sample sticks to the surface of the substrate. The floating sample can be fixed in place or guided around the surface of the water using a small metal pin. The NINT graphene comes pre-spun with a 1 μm-thick layer of PMMA, which is thick enough to allow for a dry mechanical transfer of the graphene to the target substrate. Using this method, the sample is cut to size with a scalpel in a glass

Petri dish and is carefully transferred to the substrate using tweezers. Fig. 4.1 is an optical micrograph of a silicon waveguide that has graphene/PMMA from NINT transferred onto it. The thermal nonlinear measurements described in the next chapter is done using this substrate.

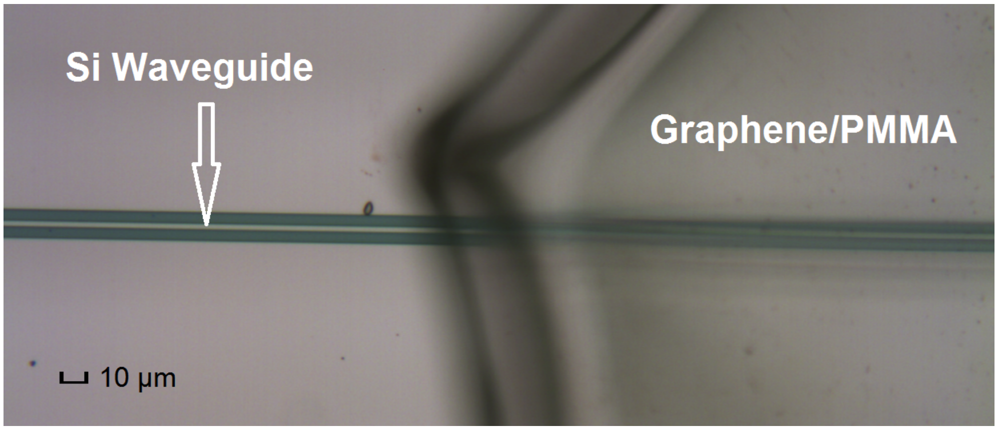

Figure 4.1: Optical micrograph of graphene/PMMA dry transferred onto a silicon substrate with a pre-patterned waveguide.

4.3 Raman spectroscopy

A common method of verifying the quality of the transferred graphene is by using Raman spectroscopy. This technique uses inelastic scattering of photons to determine information about the crystal lattice of the graphene film. When light strikes the graphene film, it excites phonons in the crystal lattice and causes the wavelength of the scattered photons to shift. This shift is plotted versus intensity to yield the Raman spectrum. Information such as the number of layers and the degree of disorder in the crystal lattice can be determined from the Raman spectrum of graphene [15]. There are three significant resonances to examine in the Raman spectrum of graphene for information about the number of layers and the level of disorder in the lattice: the **D** peak (located at $\sim$1327 cm^{-1}), **G** peak (located at $\sim$1583 cm^{-1}), and **2D** peak (located at $\sim$2700 cm^{-1}) [6]. The relative intensities of the G and 2D peaks give information on the number of layers, and the intensity of the D peak gives information about the degree of defects present in the crystal lattice. Fig. 4.2 shows a Raman spectrograph taken of a sample of graphene from NINT with the main resonances labeled. For single-layer graphene, the intensity ratio I(2D)/I(G) is much larger than 2 and can be as high as 4 [13]. The relative intensities of the G and 2D peaks in Fig. 4.2 are of comparable intensity (ratio of 1.3) which indicates that the graphene is most likely bilayer [48].

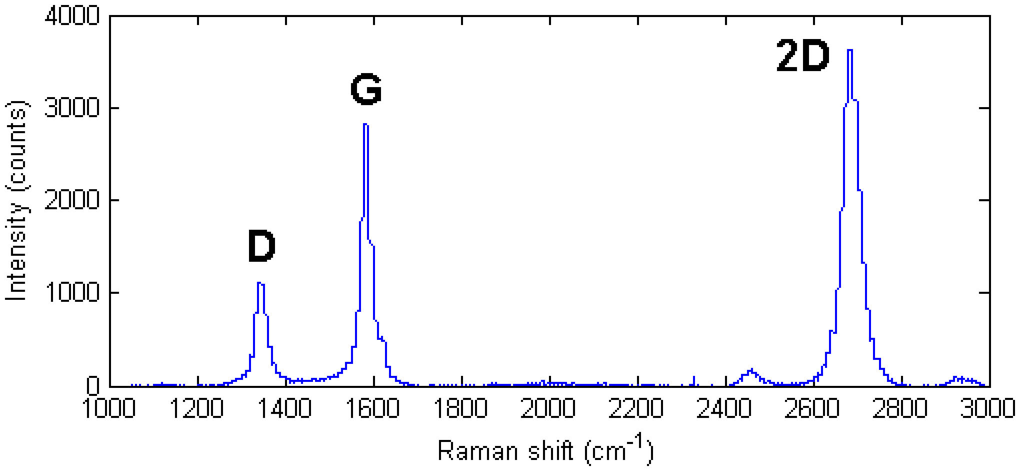

Figure 4.2: Raman spectrograph of graphene synthesized using NINT process (measured by Rob Indoe of NINT). Important resonances (D, G, 2D) indicated on plot.

The origin of the G peak arises from vibrations in the carbon-carbon bonds, and also exists for graphite. The 2D peak in graphene arises from two phonons that have opposite momentum in the highest optical phonon branch. The splitting of these phonon branches or splitting of the electronic bands for multilayer graphene and bulk graphite causes more components of the 2D peak to exist. [14] Because each component is shifted slightly in energy, this is what causes the overall intensity of the 2D peak to decrease for increasing number of layers. The D peak arises from disorder in the crystal lattice, either from performing the measurement at the edge of a sample or from measuring a sample with defects in the lattice.

4.4 Lithographic patterning of graphene

Two lithographic patterning techniques were developed using standard processes available in the University of Alberta Nanofabrication Facility (nanoFAB). After the transfer of graphene onto the substrate, patterning can be done to define features in the graphene layer. Lithographic patterning is useful for optoelectronic devices that require electrodes and specific pathways where electrons and light can interact with the graphene layer. The first method developed involves the patterning of graphene after the photonic devices have been fabricated on-chip. The second method involves patterning before the devices are fabricated.

4.4.1 Post-device patterning

Post-device patterning involves patterning the graphene layer once the photonic devices have been defined on-chip. This approach is used in various devices described in literature to pattern graphene over existing photonic features [19,29,35]. The process flow developed for post-waveguide patterning of graphene is shown in Fig. 4.3. The details are as follows:

1. Define photonic devices on Si chip using EBL and etching.
2. Transfer graphene/PMMA onto substrate and bake for adhesion.
3. Spin 1.2 μm-thick HPR504 photoresist layer on top of graphene/PMMA.
4. Expose and develop pattern into HPR504 resist.
5. Remove the exposed PMMA and graphene using O_2 plasma etch.
6. Remove HPR504 etch mask and PMMA using acetone.

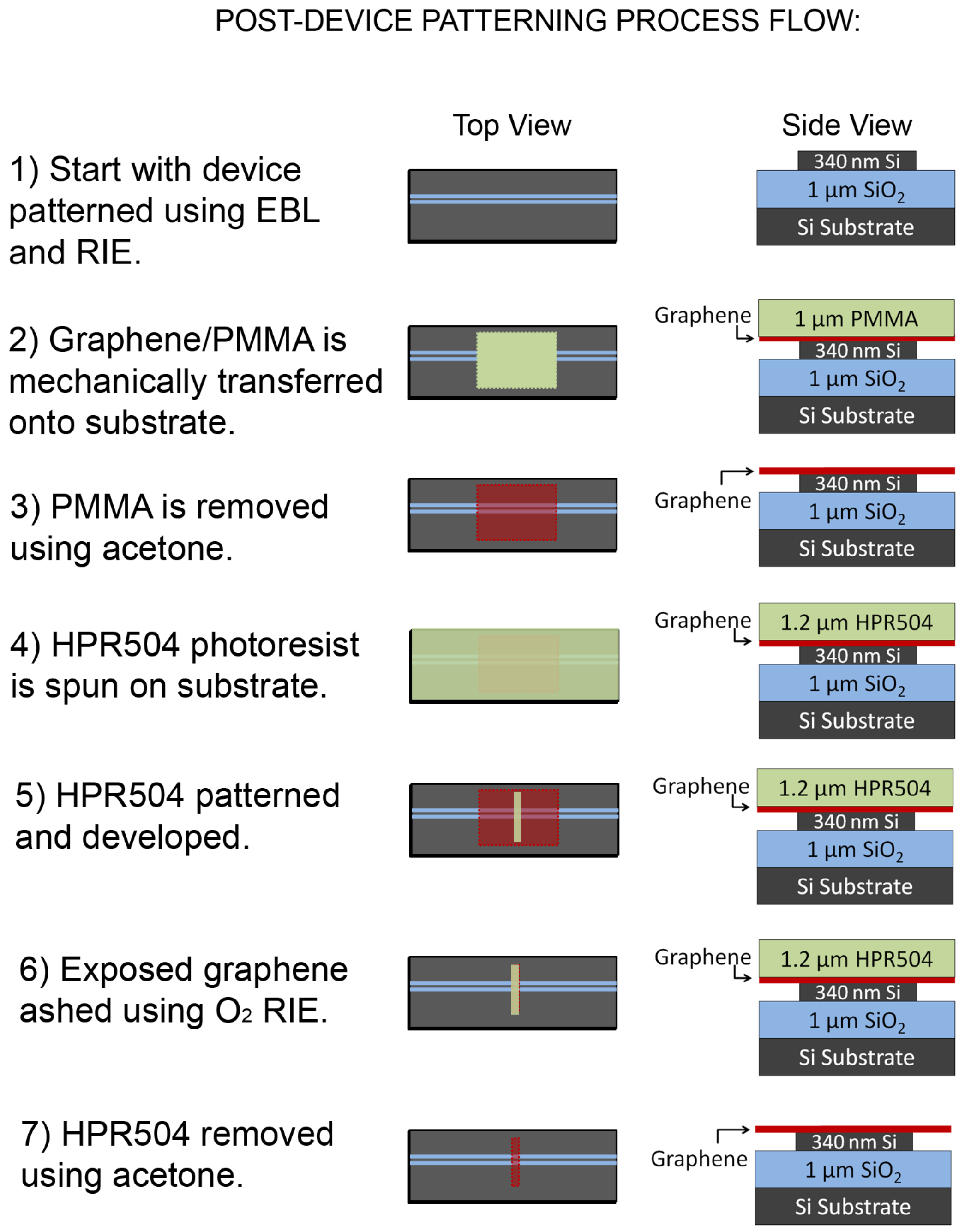
POST-DEVICE PATTERNING PROCESS FLOW:

1) Start with device patterned using EBL and RIE.

2) Graphene/PMMA is mechanically transferred onto substrate.

3) PMMA is removed using acetone.

4) HPR504 photoresist is spun on substrate.

5) HPR504 patterned and developed.

6) Exposed graphene ashed using O_2 RIE.

7) HPR504 removed using acetone.

Figure 4.3: Process flow for the post-device fabrication of graphene-silicon devices.

The transfer process used is the wet process described in the previous section. The bake step is performed to help adhere the graphene layer to the substrate and was done at 150^{o}C for 45 minutes. The temperature was chosen to be above the glass transition temperature of PMMA, allowing the PMMA to partially melt and allow the graphene layer to better shape itself over the underlying structures.

HPR504 photoresist is commonly used in the nanoFAB when patterning features using optical lithography. The procedure outlined in Appendix B was used to pattern features into the resist. This procedure has been tested for large feature sizes (greater than 10 μm) and so the procedure may need some adjustment if smaller features are required.

The next step is to remove the PMMA and graphene from the exposed regions. Both PMMA and graphene are removable using an oxygen plasma etch process. The etch recipe is developed such that the graphene and PMMA in the exposed areas are etched away, but the HPR504 etch mask remains so that it can protect the unexposed regions of graphene. To remove the PMMA and graphene, the chip was etched (using the μEtch RIE in the nanoFAB) for 3 minutes using a 80 sccm oxygen flow rate at 200 mT pressure and 100 W RF power. Fig. 4.4 is an optical micrograph of a 300 μm strip of graphene with the exposed areas etched away. The image was taken before the HPR504 and PMMA was removed.

The last step is to remove both the HPR504 and PMMA using acetone. A soak of 10 minutes with light agitation was done to dissolve the photoresist. Ultrasonic agitation should be avoided since it may cause the patterned graphene to detach from the substrate. Once this is done, patterned graphene

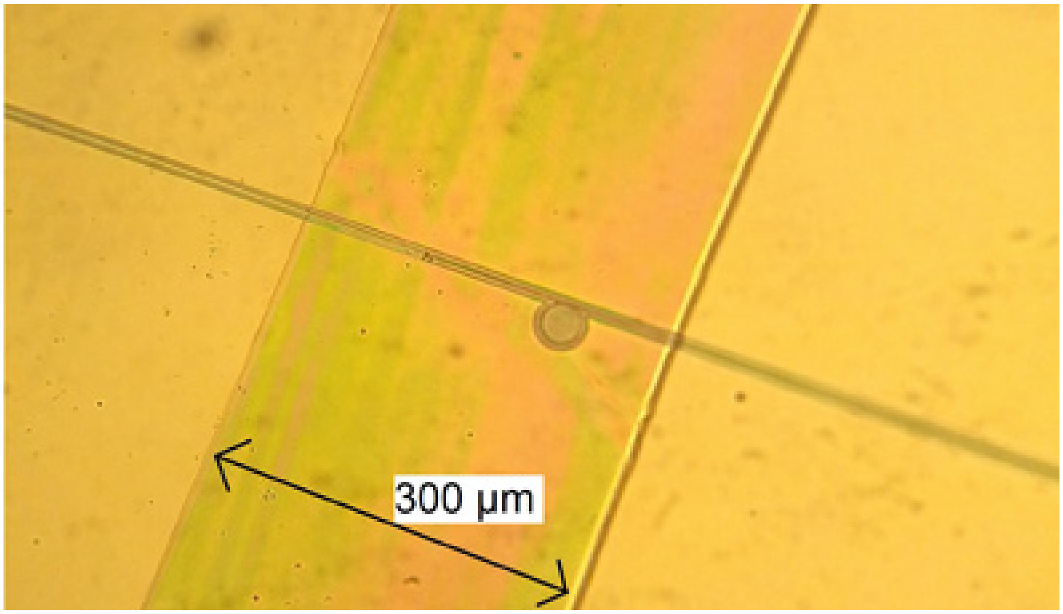

Figure 4.4: Optical micrograph of 300 μm strip of graphene patterned over an optical microring resonator and bus waveguides. HPR504 and PMMA have not yet been removed with acetone.

should remain on the chip. Because the colour contrast between graphene and silicon is very poor, a region of SiO_2 (which has much better contrast) on the edge of an SOI chip was used to optically verify the presence of graphene on the chip. Fig. 4.5 is an optical micrograph of the SiO_2 region that was used to verify that the graphene was successfully transferred and patterned. Fig. 4.6 is a scanning electron microscope (SEM) image of graphene suspended over the waveguide core after the removal of the PMMA. Without the PMMA support layer, the graphene layer is observed to buckle in the waveguide trench areas.

4.4.2 Pre-device patterning

Pre-device patterning involves transferring the graphene onto the substrate and patterning it before any of the underlying photonic features are defined. For pre-device patterning, the same steps are followed in post-device patterning, except that the patterning of the graphene is done on the SOI substrate before any devices are written. The spinning of the electron beam resist, de-

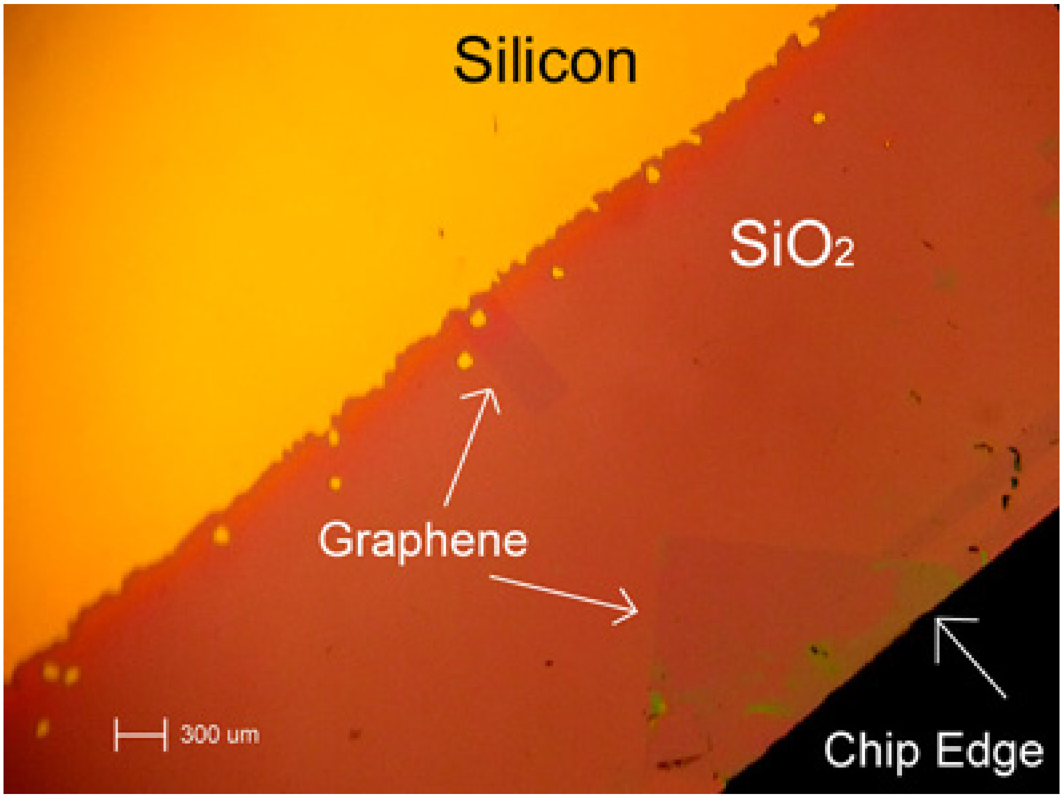

Figure 4.5: Optical micrograph of graphene patterned on an SOI chip after removal of photoresist. A faint 300 μm-wide graphene strip and alignment arrow can be seen in the SiO_2 region.

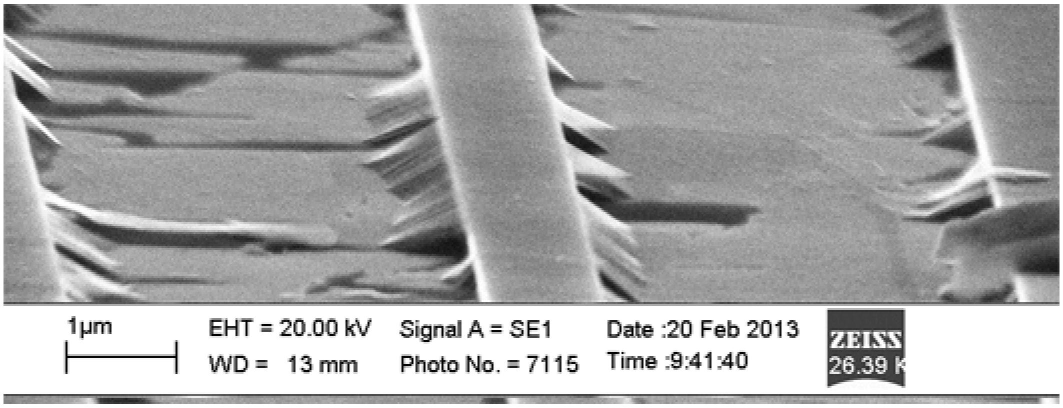

Figure 4.6: SEM image of graphene suspended over a 1 μm-wide waveguide core and two adjacent 4μm-wide trenches.

velopment and silicon etching all occur after the graphene is patterned. For structures that require a graphene layer inside the waveguiding structure, pre-waveguide patterning may be a good approach to take. Graphene devices such

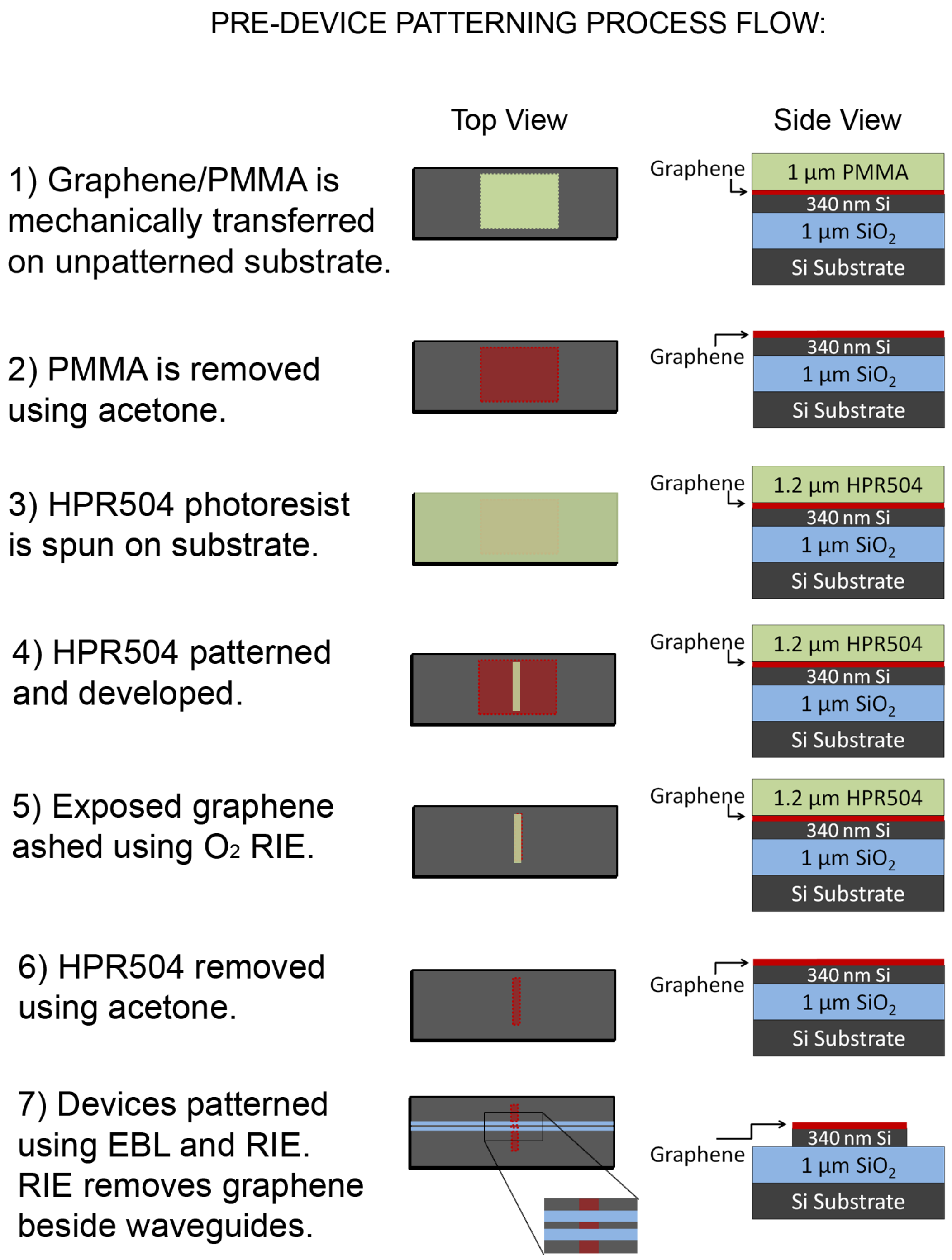

Figure 4.7: Process flow for the pre-device fabrication of graphene-silicon devices.

as the assisted coupler by Locatelli et al. [36] require that a graphene layer be defined in between two silicon regions. The silicon etch step of the device fabrication removes the graphene beside the waveguide. Therefore, pre-waveguide patterning could be done if the presence of graphene cannot be tolerated on the sides of the device. Graphene will tend to buckle across gaps when a support layer is not present (as seen in Fig. 4.6). Any buckled graphene that is in the vicinity of the waveguide core could interact with the evanescent light field and affect device performance.

The process flow is shown in Fig. 4.7. Pre-device graphene patterning was performed on an SOI substrate. After the transfer and graphene patterning was done, waveguides were then defined along the length of the chip using EBL and silicon etching. A Raman line scan was performed to confirm the presence of graphene on the waveguide core after the silicon etch. Fig. 4.8 is a colour map of the G peak intensity with position, which is used to indicate the presence of graphene on the waveguide and the absence of graphene in the adjacent trenches. The spot size of the Raman laser is approximately 700 nm and the step size of the line scan is fixed to a minimum of 1 μm/step, so this will result in some error in the widths of the Raman signal shown in the figure.

4.5 Summary

In this chapter, the methods of synthesizing graphene were briefly discussed. Both suppliers of graphene for this thesis work used the chemical vapour deposition method. Depending on the thickness of the polymer support layer, a wet or dry transfer process is used to transfer the graphene onto an SOI substrate for device fabrication. The presence and quality of the transferred graphene was verified using optical microscopy, scanning electron microscopy and Raman spectroscopy. After the transfer step, lithographic patterning of

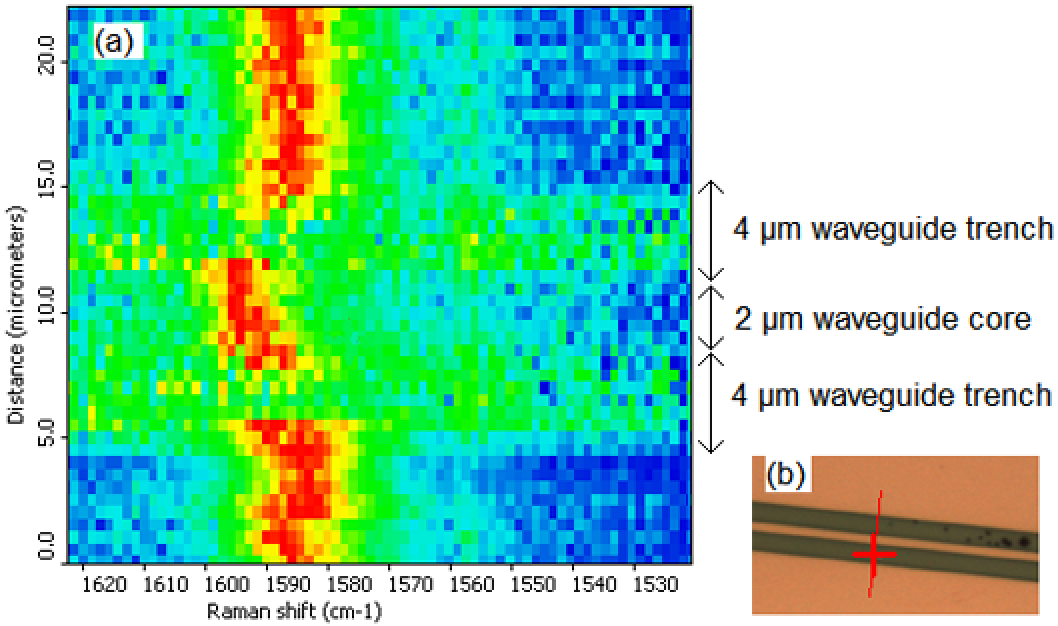

Figure 4.8: (a) Raman line scan of waveguide after pre-device graphene patterning and subsequent waveguide patterning. Red indicates a strong G peak intensity. (b) Optical micrograph of waveguide with line scan path indicated in red.

the graphene can be done. Two different techniques for patterning graphene were developed: post-device patterning and pre-device patterning. Post-device patterning involves overlaying the existing photonic devices with patterned graphene. This technique is useful for optoelectronics development where continuous paths of graphene need to be defined for electrical contact. Pre-device patterning involves transferring and patterning the graphene before the photonic devices are written on the chip. This method may be useful in realizing graphene optical waveguides which require the graphene layer to exactly conform with the waveguide geometries. In the next chapter, graphene that has been transferred onto a silicon waveguide resonator will be used to determine the waveguide propagation characteristics and thermal nonlinearity of graphene-silicon waveguides. These results will be then compared with the results of the numerical simulation from Chapter 3 and discussed.

Chapter 5

Linear and Nonlinear Characterization of Graphene-Si Waveguide

The thermal nonlinear index was estimated for a graphene-silicon waveguide using numerical simulations in Chapter 3. Using the graphene transfer process described in Chapter 4, a graphene-silicon waveguide was fabricated to explore the linear transmission and thermal nonlinear properties of the waveguide. This chapter will outline the experimental procedure for measuring the thermal nonlinearity and determining the effective nonlinear index due to thermal effects. The experimental results will then be compared to the results from the numerical simulation.

5.1 Experimental setup

The Nanophotonics Research Laboratory (located at W4-087, ECERF) is equipped with characterization equipment that allows for the spectral response of on-chip photonic devices to be measured. The apparatus is a fiber-based setup where light from a tunable infrared laser is coupled into a single-mode fiber. If high power is required, the laser light is fed to an erbium-doped fiber amplifier (EDFA), which amplifies the optical power to the desired level. Because the light from the laser is randomly linearly polarized, the light is then directed through a fiber polarization controller so that the polarization can be adjusted. The polarization is controlled through the use of paddles, which use stress-induced birefringence in the fiber to adjust the output polarization. The light is then guided to a lensed fiber tip to couple the light in free space from the fiber to the input port of the on-chip device. The alignment is done using a nanopositioning stage with piezoelectric motors. The light then propagates through the on-chip device and exits through the output port. A second lensed fiber is placed at the output port to collect the light and direct it to an InGaAs photodetector that measures the output power from the device. The tunable laser and photodetector are both connected to a computer that automates the measurement of the spectral response by sweeping the wavelength of the laser and measuring the power on the photodetector. The experimental setup is depicted in Fig. 5.1.

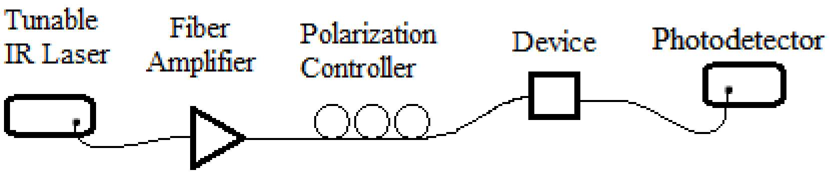

Figure 5.1: Experimental setup for measuring the spectral response of on-chip photonic devices.

The material platform that is used in the waveguide is the SOI structure described in Chapter 3. A 2 μm-wide Si waveguide with a thickness of 340 nm is pre-patterned into an SOI chip using electron beam lithography and reactive ion etching. The chip is then cleaved on both sides to provide smooth facets that act as the input/output ports of the waveguide. Graphene is then mechanically transferred onto the substrate using the dry transfer method described in Section 4.3 and the PMMA is kept on the sample for mechanical support of the graphene layer. The region of graphene/PMMA is 2.5 mmwide, with 0.4 μm-wide regions on both sides that consist of bare silicon. Fig. 5.2 is a top and cross-sectional view of the waveguide.

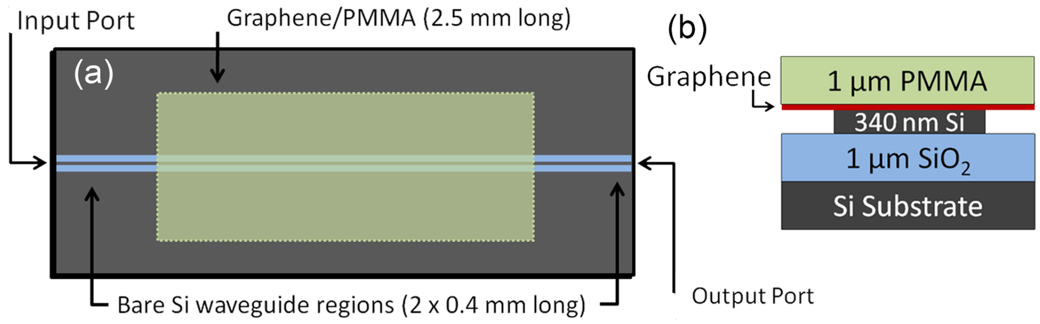

Figure 5.2: (a) Top view of graphene-silicon waveguide resonator. (b) Cross-sectional view of the graphene-silicon waveguide.

5.2 Linear resonator properties

The input and output ports of the waveguide after cleaving are reflective due to the dielectric interface between silicon and air, which causes the waveguide to act as a Fabry-Pérot resonator cavity. The effective index of the optical mode contains a linear contribution n_{eff} and an intensity-dependent portion $n_{2,eff}I$ (as shown in Eqn. 2.13). The effective nonlinear index $n_{2,eff}$ can be found by measuring the change in the effective index as a function of intensity. The spectral response of the resonator is sensitive to changes in the effective index, since the resonant wavelengths depend on the optical path length of the cavity (Eqn. 1.2) which is partly determined by the refractive index of the material. Therefore, the magnitude of the measured resonance shifts can be directly correlated to the effective index change and can be used to find $n_{2,eff}$. However, the free-spectral range (wavelength spacing between adjacent resonances) is determined by the group index. The group index and effective index of the optical mode are related by the following expression:

$$n_g = n_{eff} - \lambda\left(\frac{dn_{eff}}{d\lambda}\right) \tag{5.1}$$

The effective index n_{eff} is determined by the waveguide structure and the optical mode that is excited. The group index n_g factors in the dependence of the effective index on the wavelength (dispersion). For this experiment, it is assumed that the change in the effective index with intensity is approximately the same as the change in the group index:

$$\frac{dn_g}{dI} \approx \frac{dn_{eff}}{dI} \tag{5.2}$$

For a Fabry-Pérot resonator, the group index at wavelength λ can be calculated from the free spectral range of the resonance spectrum if the length of the cavity L is known [10]:

$$\Delta\lambda_{FSR} = \frac{\lambda^2}{2Ln_g} \tag{5.3}$$

The first step is to determine the properties of the Fabry-Pérot resonator, such as the reflectivity R of each facet and the FSR $\Delta\lambda_{FSR}$, without any graphene present. The spectral response of the device is measured using TE and TM polarization and a fit is done using the theoretical model given by Eqn. 1.1. The measured data and theoretical fit for TM polarization is shown in Fig. 5.3. From the fit, the power reflectivity of each facet was found to be R = 0.35. The FSR was measured to be 85.1 pm for TM polarization and 102.3 pm for TE, which corresponds to a group index of 4.28 and 3.56 for the TM and TE mode respectively.

5.2.1 Linear propagation loss and input power

The input power into the waveguide resonator must first be estimated using the source laser power and the power measured by the photodetector. There is coupling loss that arises from the free-space coupling of light between the tapered fibers and the facets of the device. Coupling loss is estimated by measuring the power output of the cavity at resonance without any graphene on the substrate. With negligible propagation loss, the output transmittance

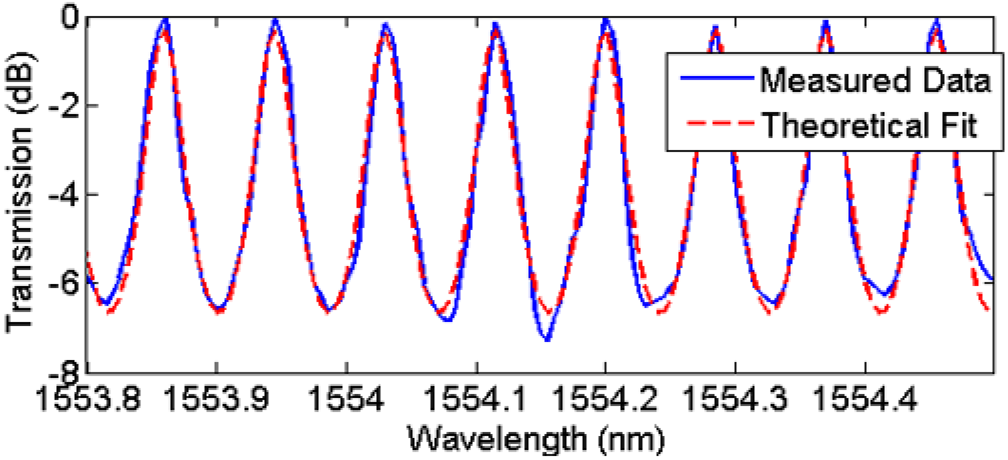

Figure 5.3: Spectral response of the Fabry-Pérot waveguide resonator for TM polarization without graphene.

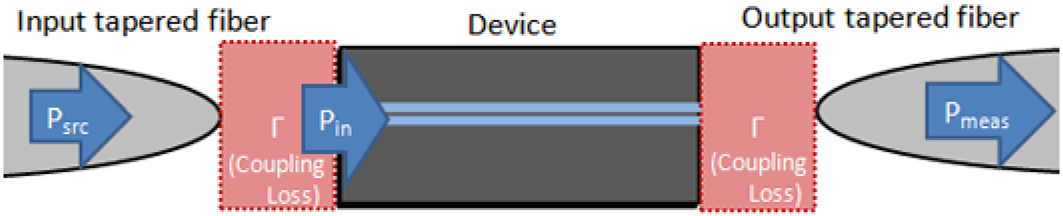

Figure 5.4: Definitions of source, input and measured power in device measurement.

of the cavity is equal to the input transmittance (by Eqn. 1.1). In this case, the only loss in the system is the coupling loss of each facet, Γ (diagram shown in Fig. 5.4):

$$P_{meas} = P_{src}\Gamma^2 \tag{5.4}$$

It is important to note that the input power P_{in} is the optical power immediately before the resonator after coupling effects have been considered. The source power P_{src} is taken from the readout of the erbium-doped fiber amplifier (EDFA). The measured power P_{meas} is calculated from the readout of an InGaAs photodetector and the efficiency of the photodetector (32%). From these measurements, the coupling loss per facet was measured to be Γ_{TM} = -13.5 dB for TM polarization, and Γ_{TE} = -14.7 dB for TE. The input power is then defined as the source power with the coupling loss of one facet applied to it:

$$P_{in} = P_{src}\Gamma \tag{5.5}$$

In Chapter 2, the optical properties of graphene show that for $\lambda_0 = 1.55$ μm, undoped graphene acts as a lossy dielectric material. Therefore, when graphene is added to the waveguide, the optical absorption of graphene will add additional loss to the measurement of P_{meas}. Assuming the same per-facet coupling losses as the bare silicon case, the transmittance of the graphene-silicon waveguide resonator was measured at resonance under low input power (500 μW). From this measurement, G was found using Eqn. 1.1 and the propagation loss was calculated to be 19.3 dB/cm for TM polarization and 9.8 dB/cm for TE polarization. These propagation losses are lower than the insertion losses measured by Kim et al. in their polymer waveguide-based polarizers without a cladding layer (30 dB/cm for TM polarization and 16 dB/cm for TE polarization using a graphene region 7 mm long) [28]. This may be because of defects in our graphene (shown in the Raman spectrum by the "D" peak in Chapter 4), or that coverage is not uniform over the entire length of waveguide. Our device has a polarization-dependent propagation loss much like this device by Kim et al. and another fiber-based polarizer by Bao et al. [4], where a 9.5 dB/cm extinction ratio exists between TM and TE polarization.

5.3 Nonlinear index measurement

By measuring the shift in the resonant wavelength for varying input power, the change in the group index (and thus, change in the effective index) can be calculated from the following relationship between the fractional change in the resonant wavelength and group index:

$$\frac{\Delta\lambda}{\lambda} = \frac{\Delta n_g}{n_g} \tag{5.6}$$

$$\Delta n_{eff} \approx \Delta n_g = \Delta\lambda\left(\frac{n_g}{\lambda}\right) \tag{5.7}$$

The intensity of light is proportional to the square of the electric field and varies according to the modal electric field distribution. As shown in Chapter 3, the effective modal area is used to calculate the intensity from the input power using Eqn. 3.31. Therefore, if the slope of the resonant wavelength shift versus input power relationship ($\Delta\lambda/\Delta P_{in}$) can be found for each case, $n_{2,eff}$ ($\Delta n_{eff}/\Delta I$) can be calculated from the slope.

5.3.1 Intracavity intensity

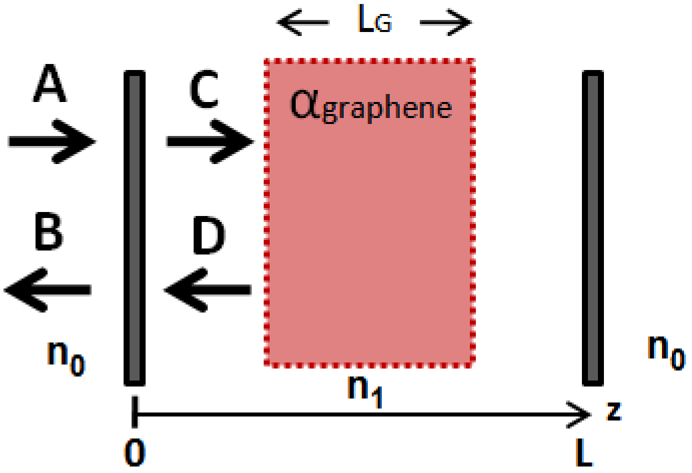

Figure 5.5: Definition of electric fields used in the derivation of the Fabry-Pérot intracavity intensity.

The intracavity intensity can be found from the input intensity and the fields inside the Fabry-Pérot cavity. The inside and outside forward/backward traveling waves are labeled in Fig. 5.5. The field A represents the input electric field into the resonator. To relate C to A, the transmission through the first interface at $z = 0$ as well as the sum of the forward travelling waves in the cavity must be considered. The wave encounters a region of lossy graphene (with absorption coefficient α) that is $L_G = 2.5$ mm long. On either side of the lossy region, bare silicon regions of length $L_{Si} = 0.4$ mm exist. The total resonator length is $L = 3.3$ mm. It is assumed that the propagation constant β in the graphene region is the same as in the bare silicon region and that no reflection occurs at the boundaries of the graphene region. Table 3.2 supports this assumption, which shows that the real part of the effective modal index is approximately the same in numerical simulations for both regions. The expression that describes the sum of the fields that make up the field C at $z = 0$ is:

$$C = At_{01} + At_{01}r_{10}^2 e^{-2\alpha L_G} e^{-2j\beta L} + At_{01}r_{10}^4 e^{-4\alpha L_G} e^{-4j\beta L} + ... \tag{5.8}$$

$$C = At_{01}(1 + r_{10}^2 e^{-2\alpha L_G} e^{-2j\beta L} + r_{10}^4 e^{-4\alpha L_G} e^{-4j\beta L} + ...) \tag{5.9}$$

where r_{10} and t_{01} are the Fresnel coefficients associated with reflection from an interface between media with index n_1 and n_0, and transmission through an interface between media with index n_0 and n_1 respectively. The power reflectance R is defined as $R = r_{01}^2 = r_{10}^2$ and power transmittance T as $T = (1 - R) = t_{01}^2 = t_{10}^2$. This infinite geometric series can be simplified to the following:

$$C = \frac{At_{01}}{(1 - r_{10}^2 e^{-2\alpha L_G} e^{-2j\beta L})} \tag{5.10}$$

At resonance, $e^{-2j\beta L} = 1$ and the expression for C simplifies even further:

$$C = \frac{At_{01}}{(1 - r_{10}^2 e^{-2\alpha L_G})} \tag{5.11}$$

The same approach can be done to find the sum of the backward travelling waves at z = 0 (field D):

$$D = At_{01}r_{10} e^{-2\alpha L_G} e^{-2j\beta L} + At_{01}r_{10}^3 e^{-4\alpha L_G} e^{-4j\beta L} + ... \tag{5.12}$$

$$D = \frac{At_{01}r_{10}e^{-2\alpha L_G}}{(1 - r_{10}^2 e^{-2\alpha L_G})} \tag{5.13}$$

The intracavity field $E(z)$ is then found from the sum of the forward and backward waves at $z = 0$ with the appropriate phase shift applied to the fields. There are three regions to consider for the device: the bare silicon regions at the input and output, and the lossy graphene region. For the first bare silicon region, only a phase shift is applied to the fields at $z = 0$:

$$E_1(z) = Ce^{-j\beta z} + De^{j\beta z} \tag{5.14}$$

For the lossy graphene region, attenuation of the C and D fields needs to be considered along with the phase shift. Because attenuation does not occur in the bare silicon region, we only factor in the region of the graphene described by the length $(z - L_{Si})$:

$$E_2(z) = Ce^{-j\beta z}e^{-\alpha(z-L_{Si})} + De^{j\beta z}e^{\alpha(z-L_{Si})} \tag{5.15}$$

For the remaining bare silicon region, the fields C and D incur a phase shift along with the attenuation from the graphene region:

$$E_3(z) = Ce^{-j\beta z}e^{-\alpha L_G} + De^{j\beta z}e^{\alpha L_G} \tag{5.16}$$

The intracavity intensity enhancement of the resonator is defined as the intensity inside the cavity, normalized by the input intensity $|A|^2$ to the resonator:

$$\frac{I(z)}{I_{in}} = \left|\frac{E(z)}{A}\right|^2 \tag{5.17}$$

Fig. 5.6 shows a plot of the spatial intracavity intensity enhancement $I(z)/I_{in}$ in the graphene-Si cavity using TM polarization with the three regions indicated. The value of $n_{2,eff}$ is estimated using the average intracavity intensity, which is found by taking the spatial average of $I(z)$ over the entire length of the cavity:

$$I_{cav} = \frac{\left[\int_0^{L_{Si}} (I_1(z))\, dz + \int_{L_{Si}}^{L_{Si}+L_G} (I_2(z))\, dz + \int_{L_{Si}+L_G}^{L} (I_3(z))\, dz\right]}{L} \tag{5.18}$$

The integrals can be solved analytically and are:

$$\int_0^{L_{Si}} (I_1(z))\ dz = \frac{(1-R)(1+Re^{-4\alpha L_G})}{(1-Re^{-2\alpha L_G})^2} L_{Si} \tag{5.19}$$

$$\int_{L_{Si}}^{L_{Si}+L_G} (I_2(z))\ dz = \frac{(1-R)(Re^{-4\alpha L_G}e^{2\alpha L_G} - e^{-2\alpha L_G} - Re^{-4\alpha L_G} + 1)}{(2\alpha)(1-Re^{-2\alpha L_g})^2} \tag{5.20}$$

$$\int_{L_{Si}+L_G}^{L} (I_3(z)) = \frac{(1-R)(e^{-2\alpha L_G} + Re^{-2\alpha L_G})}{(1-Re^{-2\alpha L_G})^2} L_{Si} \tag{5.21}$$

Using the propagation loss of the graphene-Si region for TE and TM polarization (α_{TM} = 19.3 dB/cm and α_{TE} = 9.8 dB/cm), the values for I_{cav}/I_{in} waveguide were calculated analytically and verified using trapezoidal integration in MATLAB. The values were found to be 0.573 for TM polarization and 0.923 for TE. By setting $\alpha = 0$ for the case with no graphene region, it was found to be 2.08 for TM polarization. This enhancement factor is then applied to the input intensity in the calculation for $n_{2,eff}$.

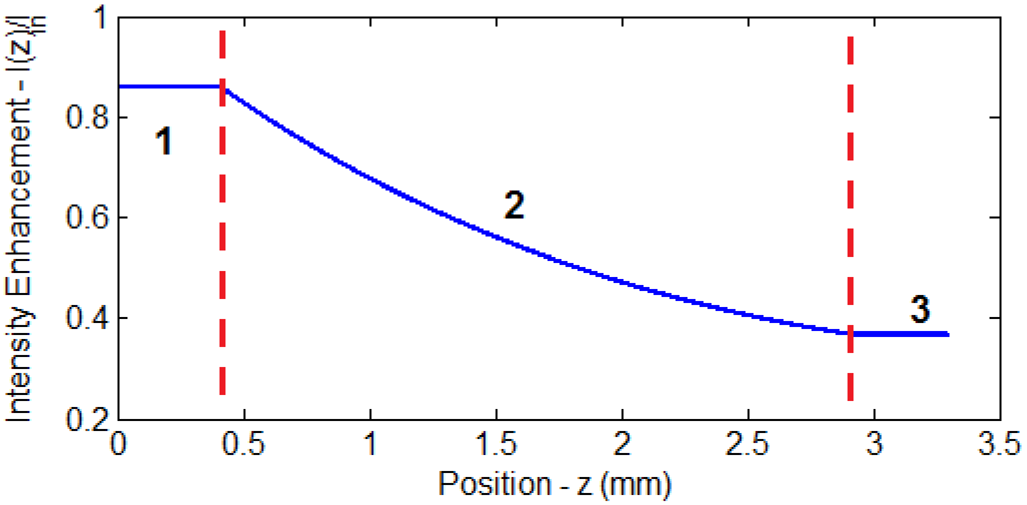

Figure 5.6: Spatial intracavity intensity (relative to the input intensity) for the three regions of the graphene-Si resonator under TM polarized light.

5.4 Experimental results

The spectral response for varying input power is shown in Fig. 5.7. As the input power is increased, the resonant wavelength of the Fabry-Pérot response experiences a red-shift. The magnitude of the shift was measured for each case, and the dependence of the shift on input power is plotted in Fig. 5.8. A linear fit is performed on the data, and the slope corresponding to $\Delta\lambda/\Delta P_{in}$ is found. For each case, the slope is multiplied by the effective modal area to get $\Delta\lambda/\Delta I_{in}$ and then divided by the intracavity enhancement factor to get $\Delta\lambda/\Delta I_{cav}$. Using Eqn. 5.2 and Eqn. 5.7, $\Delta\lambda$ is related to Δn_{eff}. Therefore, the total expression for finding n_2 is the following:

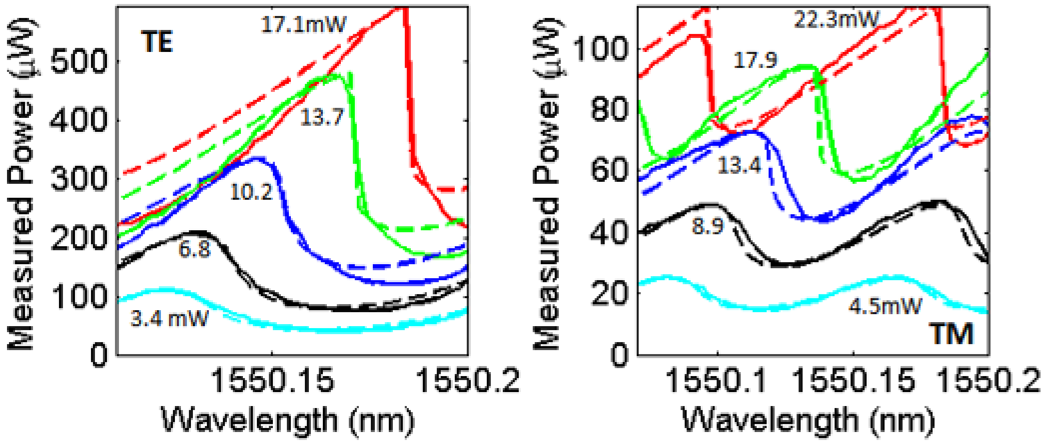

Figure 5.7: Spectral response for graphene-Si waveguide resonator at varying input power for TE and TM polarization. Solid lines are measurements and dashed lines are theoretical fits from the optical bistability model.

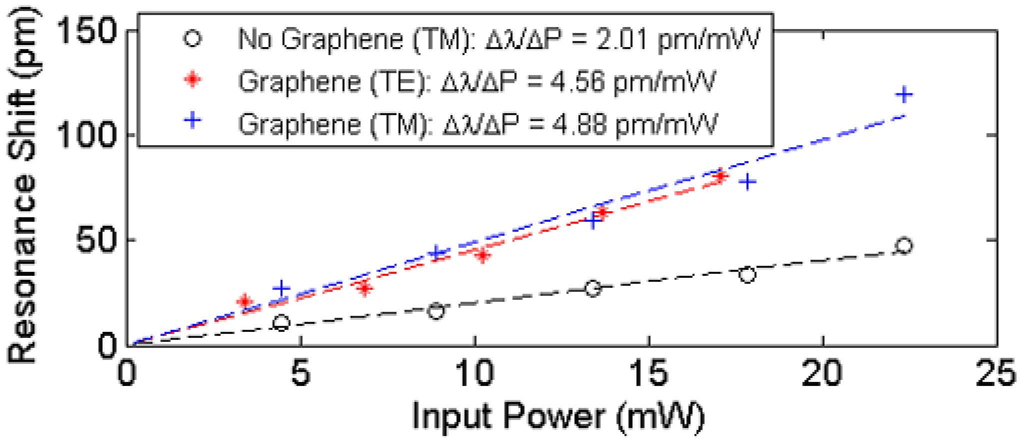

Figure 5.8: Dependence of the resonant wavelength shift on the input power (dotted lines are linear fits of the data).

$$n_{2,eff} = \left(\frac{\Delta n_{eff}}{\Delta I_{cav}}\right) = \left(\frac{\Delta\lambda}{\Delta P_{in}}\right)\left(\frac{\Delta P_{in}}{\Delta I_{in}}\right)\left(\frac{\Delta I_{in}}{\Delta I_{cav}}\right)\left(\frac{\Delta n_{eff}}{\Delta\lambda}\right) \tag{5.22}$$

$$n_{2,eff} = \left(\frac{\Delta\lambda}{\Delta P_{in}}\right)\left(\frac{I_{in}}{I_{cav}}\right)\left(\frac{n_g A_{eff}}{\lambda}\right) \tag{5.23}$$

A summary of the values used for the calculation is given in Table 5.1. The effective modal area A_{eff} and group index n_g are taken from Section 3.4 and 5.2 respectively.

Table 5.1: Calculation of Effective Thermal Nonlinear Index

	Resonance Shift vs. Input Power $\Delta\lambda/\Delta P_{in}$ **(pm/mW)**	**Intracavity Intensity Enhancement** I_{cav}/I_{in}	**Effective Nonlinear Index (10^{-11} cm^2/W)**
Graphene (TE)	4.56	0.923	5.57
Graphene (TM)	4.88	0.573	17.9
Bare Si (TM)	2.01	2.08	2.03

The results show that with the addition of graphene on a bare silicon waveguide, the effective thermal nonlinear index experiences a 8.8-fold enhancement for TM polarization. The nonlinear index associated with TE polarization is approximately three times lower than the value for TM. This can be attributed mainly to the larger tangential electric field that exists in the graphene layer for TM polarization, which results in an increased amount of ohmic heating in the graphene layer. As well, the effective modal area for the TM mode (0.760 μm^2) also differs from the area of the TE mode (0.490 μm^2), which reduces the intensity for the same input power.

The $n_{2,eff}$ from the numerical simulation in Chapter 3 and from experiment are compared in Table 5.2. It can be seen that the experimental values for

n_2 are in close agreement with the values from the simulation. The ratio between the TM and TE $n_{2,eff}$ values are nearly the same for the simulation and experiment (2.9 and 3.2 respectively). The uncertainty in the optical absorption in the silicon is likely responsible for the discrepancy between the experimental and simulation values for bare silicon.

Table 5.2: Effective Thermal Nonlinear Index n_2 from Simulation and Experiment

	Effective Nonlinear Index (10^{-11} cm^2/W) (Simulation)	**Effective Nonlinear Index (10^{-11} cm^2/W)** (Experiment)
Graphene (TE)	7.06	5.57
Graphene (TM)	20.7	17.9
Bare Si (TM)	1.26	2.03

5.4.1 Optical bistability analysis

In Fig. 5.7, asymmetry in the spectral response begins to appear at higher input powers. This is because for nonlinear media, the refractive index (and by extension, the round-trip phase delay) is a function of the input power. This allows for multiple solutions for the output power of the Fabry-Pérot resonator to exist for a given input power. The relationship between the input and output power in a nonlinear lossless Fabry-Pérot is given by the following relation [5]:

$$\frac{I_{fwd}}{I_{in}} = \frac{1/T}{1 + (4R/T^2)\sin^2(\delta(I_{cav})/2)} \tag{5.24}$$

where the round-trip phase delay is:

$$\delta(I_{cav}) = 2n_0(\omega/c)L + 2n_2 I_{cav}(\omega/c)L \tag{5.25}$$

and I_{fwd} is the intensity of the forward travelling field "C" described in section 5.3.1, R and T are the reflection and transmission coefficients of the reflector,

ω is the frequency of the light used and I_{in} is the input intensity of the cavity. This type of bistability is called "refractive bistability" and does not consider loss in the Fabry-Pérot cavity, so this relation cannot be used as-is to analyze our structure. Another type of bistability exists, called "absorptive bistability", where an intensity-dependent absorption coefficient causes there to be two solutions for the output power. In our case, we are assuming that the linear absorption is predominant over any intensity-dependent losses such as two-photon absorption or free-carrier absorption. However, the bistability relation needs to be derived to include linear loss into the response. We start with the average intracavity intensity shown in Eqn. 5.18. Off-resonance, the denominator changes from $(1 - Re^{-2\alpha L_G})^2$ to $[(1 - Re^{-2\alpha L_G})^2 + 4R\sin^2(\delta(I_{cav})/2))]$. For $\delta \neq 2m\pi$, where m is an integer, the intracavity intensity as well as the output intensity is reduced from its maximal value.

In order to model the asymmetric contour of the spectral response, the two possible solutions for the cavity intensity for a given input intensity are solved numerically for each wavelength point. One of the two solutions, corresponding to a specific direction on the input vs. output power hysteresis loop, is selected. The points are then normalized and plotted alongside the experimental spectral response for each input power (see Fig. 5.7). The parameters $n_{2,eff}$ and α are found by adjusting the parameters such that the resonant wavelength shift and contour of the curve match. For each input power, the values of $n_{2,eff}$ and α will vary slightly and so the average from the five fits is taken for each polarization. The average $n_{2,eff}$ values were found to be 5.41×10^{-11} cm^2/W for TE polarization and 1.78×10^{-10} cm^2/W for TM. These values very closely agree to the values found from the linear fit using the resonance wavelength shifts alone. The average values of α found are 8.6 dB/cm and 17.7 dB/cm for TE and TM polarization respectively. These values are slightly lower but still closely agree to the measured α at low power.

5.5 Other nonlinear effects

The $n_{2,eff}$ value that we measure from experiment is a combination of all of the nonlinear effects that occur in the graphene-silicon material system. There are a number of other nonlinear effects in graphene and silicon that can contribute towards this value, such as two-photon absorption (TPA), free-carrier dispersion (FCD) and third-order Kerr nonlinearity. However, it will be demonstrated that thermal nonlinearity is predominant in the case of using a continuous-wave laser source at the intensities we are working in.

5.5.1 Two-photon absorption

Two-photon absorption exists in materials where electron transitions allow for the photoexcitation of an electron using a photon pair. Both graphene and silicon have a nonlinear absorption described by the following equation, where β_{TPA} is the two-photon absorption coefficient [5]:

$$\alpha = \alpha_0 + \beta_{TPA} I \tag{5.26}$$

The largest intracavity intensity that we are working at in this experiment is approximately 6.2 MW/cm^2. The change in the absorption coefficient of silicon from TPA using $\beta_{TPA} = 1.5$ cm/GW [7] (for $\lambda_0 = 1.55\mu$m) is $\Delta\alpha = 10^{-2}$ cm^{-1}. Considering that a loss of 1 dB/cm is approximately $\alpha = 10^{-1}$ cm^{-1}, the effect of TPA is small in this regime. For this reason, it is likely that the dominant mechanism behind optical absorption in the silicon core is linear loss from free-carrier absorption (intraband absorption) and collisions with dopants and impurities, since p+ doped SOI wafers are used.

The TPA coefficient of monolayer graphene is $\beta_{TPA} = 25$ cm/GW [19], much larger than that of silicon. However, the intensity of the optical mode in the vicinity of the graphene layer is lower than in the silicon core (by approximately four times, from numerical simulations). Therefore, this would cause a maximum shift of $\Delta\alpha = 4 \times 10^{-2}$ cm^{-1} in the absorption coefficient of graphene, which is negligible compared to the linear loss of graphene. It is interesting to note that the TPA coefficient of bilayer graphene was found by Yang et al. to be $\beta_{TPA} \approx 10^5$ cm/GW [49], many times larger than that of monolayer graphene. In the intensity regime of this experiment, this giant value would cause noticable changes to the absorption of graphene for higher power ($\Delta\alpha \approx 10^2$ cm^{-1}). However, this value was measured using epitaxially-grown graphene of much higher quality than the CVD-grown samples used in the experiment. No significant difference in the propagation loss was observed for increasing power, and so it is assumed that two-photon absorption does not play a large role in the observed nonlinearity.

5.5.2 Free-carrier dispersion

Free-carrier dispersion (FCD) arises from a refractive index change in the material due to the presence of free charge carriers. Free-carrier dispersion induces a blue-shift in the observed resonance shift [47], as opposed to the red-shift that is observed in this experiment. Therefore, free-carrier dispersion cannot be the dominant mechanism behind the observed nonlinearity. In the work of Xu et al. [47], it has been shown that free-carrier dispersion can overcome thermal nonlinear effects in a microring resonator if a pulsed laser source is used instead of a continuous-wave laser source. The pulse width of the laser must be at a rate faster than the thermal response time of the device (which is on the order of microseconds).

5.5.3 Kerr nonlinearity

In Chapter 2, the Kerr nonlinearity of silicon and graphene was briefly discussed. The effective Kerr nonlinear coefficient $n_{2,eff}$ for a graphene-silicon photonic crystal cavity was found to be 4.8×10^{-13} cm^2/W [19]. This is two orders of magnitude lower than the effective nonlinear index we measure experimentally, so it is likely that Kerr nonlinearity plays a very small role compared to thermal effects in the observed nonlinearity.

5.6 Summary

In this chapter, the nonlinear behaviour of a graphene-silicon waveguide resonator was investigated. For varying input power from a fiber amplifier, the wavelength shift of the resonance spectrum of a graphene-silicon Fabry-Pérot waveguide resonator was measured. The change in the effective refractive index was related to the wavelength shift using the definition of the group index, and the average intracavity intensity was found using the input power. Using these two pieces of information, the effective nonlinear refractive index $n_{2,eff}$ was found for the case of graphene-on-silicon and bare silicon. A 8.8-fold increase in the effective nonlinear index was observed with the addition of graphene for TM polarization. The calculated $n_{2,eff}$ values were compared with the results from the numerical simulations performed in Chapter 3 and are found to be in close agreement. Other sources of nonlinearity were briefly examined, such as two-photon absorption, free-carrier absorption and Kerr nonlinearity. It was found that the observed nonlinearity is predominantly thermal in origin.

The demonstrated enhancement in the thermal nonlinearity is useful in designing switches. Namely, all-optical switches can be designed whereby light from a pump laser induces a refractive index changes in the material so that the resonance wavelength of a resonator is detuned from its original value. If light from a weaker probe laser is then tuned to the resonant wavelength, the pump signal can modulate the transmission of the probe signal by altering the resonance [40].

Chapter 6

Conclusions and Future Directions

6.1 Thesis summary

As more types of graphene photonic devices are developed, they will rely more on graphene's unique and useful optical properties such as its tunable absorption, polarization-dependent properties, low dispersion, and nonlinear properties. This thesis work gives an overview into graphene's basic optical properties and some of the important nonlinear optical phenomena that exist in a graphene-based material system. Because silicon is a very common material platform to use for integrated photonic devices, the focus of the work was placed on graphene-silicon waveguides.

Numerical simulations were performed to examine the propagation characteristics of light in a graphene-silicon waveguide and model the heating that occurred in the device. The simulation modeled both graphene and silicon as heat sources that use the electric field information from the optical simulation to perform a steady-state thermal simulation. It was found that the attenuation in the waveguide and the amount of heating was highly dependent on the polarization of light used and whether graphene was present or not. A calculation of the effective thermal nonlinear index $n_{2,eff}$ was done based on the intensity of the propagating mode and the peak temperature rise in the silicon waveguide core. To experimentally investigate the linear propagation characteristics of graphene-silicon waveguides, graphene was synthesized by researchers at NINT and was transferred onto an existing silicon waveguide that was fabricated on an SOI substrate. Some work on pre-waveguide and post-waveguide lithographic patterning was done with graphene synthesized by ACS Material.

The graphene-silicon waveguide was characterized and the linear propagation loss and nonlinear photothermal properties were measured. The propagation loss of the device was 9.8 dB/cm for TE polarization and 19.3 dB/cm for TM polarization. The observed propagation loss is lower than the loss that was observed in a graphene-polymer waveguide fabricated by Kim et al. [29]. This discrepancy was attributed to quality differences and potential differences in coverage. The waveguide also demonstrated the same polarization-dependent loss behaviour as their device and another by Bao et al. Due to the reflective input and output facets of the waveguide, the waveguide acts as a Fabry-Pérot waveguide resonator. Using the resonance spectrum of the resonator, the effective nonlinear index of refraction due to self heating was measured. The experiment involved varying the intracavity intensity and calculating the change in the effective refractive index of the material from the resonant wavelength shift. A 8.8-fold enhancement in the effective nonlinear index was demonstrated with the addition of graphene to the waveguide resonator. In addition, the measured nonlinear indices closely agree with the results from the numerical simulation. After examining other potential sources of the observed nonlinearity, it was determined that the nonlinearity is predominantly thermal in origin. To the knowledge of the author of this thesis (and associated colleagues), this work represents the first in-depth analysis of thermal nonlinearity in graphene-silicon waveguides.

6.2 Future research directions

6.2.1 Photothermal switching

Photothermal switching can occur in a graphene-silicon waveguide resonator if a second weaker light signal is coupled into the device. The stronger "pump" signal would be responsible for shifting the resonant wavelength of the resonator via. ohmic heating and the thermo-optic effect. If the wavelength of a second light signal (called the "probe" signal) is tuned to a resonance, the pump signal can modulate the probe signal by varying the intensity. The intensity of the probe signal should be much lower than the pump so that the optical properties of the resonator are only modified predominantly by the stronger pump signal. Photothermal switching has been demonstrated by our research group in polymer plasmonic microring resonators [40] in the past.

6.2.2 Thermal response time

The time it takes for the waveguide temperature to reach steady-state depends on the thermal conductivity and heat capacity of the waveguide materials [1]. For applications where temperature needs to respond rapidly to changes in intensity (such as in photothermal switching) or where quick thermal reconfiguration of devices is required, the thermal response time becomes an important parameter to optimize. It is expected that graphene's very large thermal conductivity will give rise to the development of thermo-optic devices with low thermal response times. For high-speed switching, other electronic nonlinear effects with very fast response time (in picosecond or femtosecond regime [33]) need to be used.

6.2.3 Kerr nonlinearity

A significant source of nonlinearity in graphene-silicon waveguides is Kerr nonlinearity [19], which arises from the large third-order nonlinear susceptibility of the material. Performing experiments to measure and utilize the Kerr nonlinearity of graphene can be done using a pulsed laser source as shown by Gu et al. This is because the thermal response time is much slower than the response time associated with the Kerr effect [33], and so the device cannot respond quickly enough to thermal changes but can to electronic changes. The Nanophotonics Research Laboratory is equipped with femtosecond and picosecond pulsed lasers, along with a high-speed photodetector, which could enable these experiments to be done in the future.

6.2.4 Athermal waveguide design

Thermal nonlinearity may be detrimental to devices that require the optical properties of the waveguide to be stable over the entire range of operation, such as in electro-optic modulators. For instance, heating can occur in these devices if they rely on optical absorption to modulate the output. This would slowly change the refractive index of the materials being used and potentially cause unpredictable behaviour. Athermal waveguide design is a technique that is widely used where matching materials that have a positive thermo-optic coefficient with negative T-O materials causes the net change in the effective refractive index to be zero [43]. Switching optical signals at a rate much faster than the thermal response time of the device could also mitigate heating effects, since the thermal energy dissipation will be minimized.

Bibliography

[1] A. H. Atabaki, E. Shah Hosseini, A. A. Eftekhar, S. Yegnanarayanan, and A. Adibi, “Optimization of metallic microheaters for high-speed reconfigurable silicon photonics.” *Optics Express*, vol. 18, no. 17, pp. 18 312–23, Aug. 2010.

[2] P. Avouris and C. Dimitrakopoulos, “Graphene: synthesis and applications,” *Materials Today*, vol. 15, no. 3, pp. 86–97, Mar. 2012.

[3] A. Balandin, S. Ghosh, W. Bao, I. Calizo, D. Teweldebrhan, F. Miao, and C. N. Lau, “Superior thermal conductivity of single-layer graphene,” *Nano Letters*, vol. 8, no. 3, pp. 902–7, Mar. 2008.

[4] Q. Bao, H. Zhang, B. Wang, Z. Ni, C. Lim, Y. Wang, D. Y. Tang, and K. P. Loh, “Broadband graphene polarizer,” *Nature Photonics*, vol. 5, pp. 411–415, 2011.

[5] R. Boyd, *Nonlinear Optics*, 3rd ed., 2008.

[6] M. O. Brien and B. Nichols, “CVD Synthesis and Characterization of Graphene Thin Films,” Army Research Laboratory, Tech. Rep. January, 2010.

[7] A. D. Bristow, N. Rotenberg, and H. M. van Driel, “Two-photon absorption and Kerr coefficients of silicon for 850-2200 nm,” *Applied Physics Letters*, vol. 90, no. 19, 191104, 2007.

[8] J. M. Cariou, J. Dugas, L. Martin, and P. Michel, “Refractive-index variations with temperature of PMMA and polycarbonate.” *Applied Optics*, vol. 25, no. 3, pp. 334–6, Feb. 1986.

[9] CVI Melles Griot, *CVI Melles Griot Technical Guide*, 2009.

[10] D. Duchesne, P. Cheben, R. Morandotti, B. Lamontagne, D. Christodoulides, D. X. Xu, and S. Janz, “Group-index birefringence and loss measurements in silicon-on-insulator photonic wire waveguides,” *Optical Engineering*, vol. 46, no. 10, 104602, Oct. 2007.

[11] L. A. Falkovsky, “Optical properties of graphene,” *Journal of Physics: Conference Series*, vol. 129, 01200, Oct. 2008.

[12] I. Ferain, C. A. Colinge, and J.-P. Colinge, “Multigate transistors as the future of classical metal-oxide-semiconductor field-effect transistors.” *Nature*, vol. 479, no. 7373, pp. 310–6, Nov. 2011.

[13] A. C. Ferrari, J. C. Meyer, V. Scardaci, C. Casiraghi, M. Lazzeri, F. Mauri, S. Piscanec, D. Jiang, K. S. Novoselov, S. Roth, and A. K. Geim, “Raman Spectrum of Graphene and Graphene Layers,” *Physical Review Letters*, vol. 97, no. 18, 187401, Oct. 2006.

[14] A. C. Ferrari, “Raman spectroscopy of graphene and graphite: Disorder, electron-phonon coupling, doping and nonadiabatic effects,” *Solid State Communications*, vol. 143, no. 1-2, pp. 47–57, Jul. 2007.

[15] A. C. Ferrari and D. M. Basko, “Raman spectroscopy as a versatile tool for studying the properties of graphene.” *Nature Nanotechnology*, vol. 8, no. 4, pp. 235–46, Apr. 2013.

[16] M. Fox, *Optical Properties of Solids*, 2nd ed. Oxford University Press, 2010.

[17] D. K. Gramotnev and S. I. Bozhevolnyi, “Plasmonics beyond the diffraction limit,” *Nature Photonics*, vol. 4, no. 2, pp. 83–91, Jan. 2010.

[18] A. Grieco, B. Slutsky, D. Tan, S. Zamek, M. Nezhad, and Y. Fainman, “Optical bistability in a silicon waveguide distributed Bragg reflector Fabry–Perot resonator,” *Journal of Lightwave Technology*, vol. 30, no. 14, pp. 2352–2355, 2012.

[19] T. Gu, N. Petrone, J. McMillan, A. van der Zande, M. Yu, G. Q. Lo, D. L. Kwong, J. Hone, and C. W. Wong, “Regenerative oscillation and four-wave mixing in graphene optoelectronics,” *Nature Photonics*, vol. 6, pp. 554–559, 2012.

[20] Z. Han, P. Zhang, and S. Bozhevolnyi, “Calculation of bending losses for highly confined modes of optical waveguides with transformation optics,” *Optics Letters*, vol. 38, no. 11, pp. 1778–1780, 2013.

[21] G. Hanson, “Dyadic Green’s functions for an anisotropic, non-local model of biased graphene,” *Antennas and Propagation, IEEE Transactions on*, vol. 56, no. 3, pp. 747–757, 2008.

[22] E. Hecht, *Optics*, 4th ed., 2001.

[23] Intel Corporation, “The 50G Silicon Photonics Link,” Tech. Rep., 2010.

[24] N. Izhaky, M. Morse, S. Koehl, O. Cohen, D. Rubin, A. Barkai, G. Sarid, R. Cohen, and M. J. Paniccia, “Development of CMOS-compatible integrated silicon photonics devices,” *Selected Topics in Quantum Electronics, IEEE Journal of*, vol. 12, no. 6, pp. 1688–1698, 2006.

[25] M. Jablan, H. Buljan, and M. Soljačić, “Plasmonics in graphene at infrared frequencies,” *Physical Review B*, vol. 80, no. 24, 245435, Dec. 2009.

[26] Z. Jacob, *Lecture Notes, ECE 671 (Nonlinear Optics)*. University of Alberta, 2011.

[27] J. Kang, D. Shin, S. Bae, and B. H. Hong, “Graphene transfer: key for applications.” *Nanoscale*, vol. 4, no. 18, pp. 5527–37, Sep. 2012.

[28] J. T. Kim and C.-G. Choi, “Graphene-based polymer waveguide polarizer.” *Optics Express*, vol. 20, no. 4, pp. 3556–62, Feb. 2012.

[29] J. T. Kim and S.-Y. Choi, "Graphene-based plasmonic waveguides for photonic integrated circuits." *Optics Express*, vol. 19, no. 24, pp. 24 557–62, Nov. 2011.

[30] A. V. Krasavin and A. V. Zayats, "Silicon-based plasmonic waveguides." *Optics Express*, vol. 18, no. 11, pp. 11 791–9, May 2010.

[31] H. Li, Y. Anugrah, S. J. Koester, and M. Li, "Optical absorption in graphene integrated on silicon waveguides," *Applied Physics Letters*, vol. 101, no. 11, 111110, 2012.

[32] I.-T. Lin, "Optical Properties of Graphene from the THz to the Visible Spectral Region," MSc Thesis, University of California: Los Angeles, 2012.

[33] Q. Lin, O. J. Painter, and G. P. Agrawal, "Nonlinear optical phenomena in silicon waveguides: modeling and applications." *Optics Express*, vol. 15, no. 25, pp. 16 604–44, Dec. 2007.

[34] A. Liu, L. Liao, Y. Chetrit, J. Basak, H. Nguyen, D. Rubin, and M. Paniccia, "Wavelength Division Multiplexing Based Photonic Integrated Circuits on Silicon-on-Insulator Platform," *IEEE Journal of Selected Topics in Quantum Electronics*, vol. 16, no. 1, pp. 23–32, 2010.

[35] M. Liu, X. Yin, E. Ulin-Avila, B. Geng, T. Zentgraf, L. Ju, F. Wang, and X. Zhang, "A graphene-based broadband optical modulator." *Nature*, vol. 474, no. 7349, pp. 64–7, Jun. 2011.

[36] A. Locatelli, A.-D. Capobianco, M. Midrio, S. Boscolo, and C. De Angelis, "Graphene-assisted control of coupling between optical waveguides." *Optics Express*, vol. 20, no. 27, pp. 28 479–84, Dec. 2012.

[37] S. Mikhailov, "Frequency Mixing Effects in Graphene," in *Physics and Applications of Graphene - Theory*, 2011, no. 1, pp. 519–534.

[38] M. Nakamura and L. Hirasawa, "Electric transport and magnetic properties in multilayer graphene," *Physical Review B*, vol. 77, no. 4, 045429, 2008.

[39] K. S. Novoselov, A. K. Geim, S. V. Morozov, D. Jiang, Y. Zhang, S. V. Dubonos, I. V. Grigorieva, and A. A. Firsov, "Electric field effect in atomically thin carbon films." *Science*, vol. 306, no. 5696, pp. 666–9, Oct. 2004.

[40] D. Perron, M. Wu, C. Horvath, D. Bachman, and V. Van, "All-plasmonic switching based on thermal nonlinearity in a polymer plasmonic microring resonator." *Optics Letters*, vol. 36, no. 14, pp. 2731–3, Jul. 2011.

[41] D. M. Pozar, *Microwave Engineering*, 3rd ed. Wiley, 2009.

[42] A. M. Prabhu, "Advanced Silicon Microring Resonator Devices for Optical Signal Processing," Ph.D. dissertation, University of Alberta, 2012.

[43] V. Raghunathan, W. N. Ye, J. Hu, T. Izuhara, J. Michel, and L. Kimerling, "Athermal operation of silicon waveguides: spectral, second order and footprint dependencies." *Optics Express*, vol. 18, no. 17, pp. 17 631–9, Aug. 2010.

[44] C. Tabert and E. Nicol, “Dynamical conductivity of AA-stacked bilayer graphene,” *Physical Review B*, vol. 86, no. 7, 075439, 2012.

[45] University of Alberta nanoFAB, *HPR 504 Photoresist Recipe*, 2011.

[46] V. Van, *Lecture Notes, ECE 570 (Computational Electromagnetics)*. University of Alberta, 2011.

[47] Q. Xu and M. Lipson, “Carrier-induced optical bistability in silicon ring resonators.” *Optics Letters*, vol. 31, no. 3, pp. 341–3, Feb. 2006.

[48] Z. Yan, Z. Peng, Z. Sun, J. Yao, Y. Zhu, Z. Liu, P. M. Ajayan, and J. M. Tour, “Growth of bilayer graphene on insulating substrates,” *ACS Nano*, vol. 5, no. 10, pp. 8187–8192, 2011.

[49] H. Yang, X. Feng, Q. Wang, H. Huang, W. Chen, A. T. S. Wee, and W. Ji, “Giant two-photon absorption in bilayer graphene.” *Nano Letters*, vol. 11, no. 7, pp. 2622–7, Jul. 2011.

[50] X. Zhang and Z. Liu, “Superlenses to overcome the diffraction limit.” *Nature Materials*, vol. 7, no. 6, pp. 435–41, Jun. 2008.

Appendix A

Code for COMSOL Multiphysics Simulation

Below is the MATLAB code used to determine the 2D steady-state temperature distribution for a graphene-silicon waveguide using COMSOL. The first part of the simulation determines the optical properties of the mode and the normalized modal electric field distribution. The electric field data is then provided to the thermal simulation which models the graphene and silicon as heat sources, and determines the steady-state peak temperature distribution. The effective modal area is also computed using this script.

```
eigval = 2; % Select eigenvalue (2=TM, 5=TE)
p_in = 5e-3; % 5 mW input power

format long
% Perform eigenvalue simulation of modes.
% The femeig code is autogenerated from COMSOL.
fem.sol=femeig(fem, ...
               'complexfun','on', ...
               'solcomp',{'tExEy10','tExEy20','tExEy21','ez'}, ...
               'outcomp',{'tExEy10','tExEy20','tExEy21','ez'}, ...
               'blocksize','auto', ...
               'neigs',5, ...
               'shift',-1.418784e7*i, ...
               'maxeigit',1000);

% Find total integrated power of mode.
m = sqrt(postint(fem, 'normPoav_rfwv', 'solnum', eigval));
t = postint(fem, 'conj(Ex)*Ex+conj(Ey)*Ey+conj(Ez)*Ez', 'solnum', eigval);
```

```
b = postint(fem, '(conj(Ex)*Ex+conj(Ey)*Ey+conj(Ez)*Ez)^2', 'solnum', eigval);
aeff = t^2/b;    % Effective area

% Reassemble solution matrix using normalized fields.
fem.sol = femsol(fem.sol.u.*sqrt(p_in)./m, 'lambda', fem.sol.lambda);
fem1=fem;

% Set up steady-state temperature simulation.
sol1 = asseminit(fem1, 'init', fem1, 'solnum', eigval);
fem.sol=femstatic(fem, ...
'init',sol1, ...
'solcomp',{'T'}, ...
'outcomp',{'T','tExEy10','tExEy20','tExEy21','ez'});
fem.sol = femsol([fem.sol.u fem.sol.u fem.sol.u fem.sol.u fem.sol.u], 'lambda', fem1.sol.lambda);
fem0=fem1;

% Plot values.
postplot(fem, 'tridata', 'T');
eigs = (fem.sol.lambda.*1i/(2*pi/1.55e-6));
fprintf('neff_rfwv: %f, Total power in mode (mW): %f\n', eigs(eigval), postint(fem, 'normPoav_rfwv', 'solnum', eigval)*1e3);
fprintf('attenuation (dB/cm) = %g, max T: %f\n',-4.343e-2*imag(eigs(eigval))*(2*pi/1.55e-6), postmax(fem, 'T'))
```

Appendix B

HPR504 Photoresist Recipe

The HPR504 photoresist recipe for graphene patterning is shown below. It is based on the suggestions given in the standard operating procedure provided by the University of Alberta nanoFAB [45].

1. Pour approx. 5 mL of HPR504 photoresist into a clean beaker.
2. Place the chip on the vacuum spinner and, using a pipette, disperse four drops of photoresist on each corner of the chip.
3. Spread resist at 500 rpm for 10 seconds, then spin at 4000 rpm for 40 seconds.
4. Bake chip at 115^{o}C in vacuum hotplate for 90 seconds.
5. Let chip rest for 15 minutes for re-hydration.
6. Expose photoresist under UV light using mask aligner for 3.5 seconds.
7. Submerge chip in 354 developer and lightly agitate until the removal of resist starts to be seen. Leave in for 5 more seconds, and do not exceed 20 seconds of total development time.
8. Submerge in water and lightly agitate for approx. 15 seconds to rinse any residual developer from chip. Dry gently using compressed N_2 gas.
9. Inspect features under optical microscope and re-develop if necessary.

Appendix C

Apparatus for Measuring Light Transmission in Bulk Material

As a side project, an optical setup was designed to focus light from a fiber-to-free-space collimator to a single point in free space to study light transmission through a bulk medium. High intensities are necessary to study many nonlinear effects, and so the light should be focused to as small of a point as possible to maximize the intensity in the material.

An existing fiber collimator (Thorlabs part # F240APC-1550) and objective lens (Edmund Optics part # NT46-146) was used in the design. The fiber collimator yields a collimated beam of diameter 1.6 mm, which needs to be directed into the aperture of the objective lens of diameter 8.4 mm. The focal point of the objective lens is where the light will be focused in the material. The objective lens is an infinity-corrected apochromatic objective lens with 50X magnification and a working distance of 13 mm. To minimize the spot size of the focused light, the beam diameter entering the aperture of the objective lens should be as large as possible. To do this, a beam expander is designed to maximally expand the beam from the fiber collimator without any significant spherical abberation. An in-situ imaging setup is also designed such that the sample can be brought to focus using a CCD camera.

To optimize the spot size, the ideal magnification of the beam diameter should be:

$$\frac{D_2}{D_1} = \frac{8.4 \text{ mm}}{1.6 \text{ mm}} = 5.25 \tag{C.1}$$

The Galilean configuration of beam expander, consisting of single plano-concave and plano-convex lenses, is chosen for a more compact design compared to the Keplerian configuration which makes use of two convex lenses with longer focal lengths [9]. The ratio between the focal lengths of the plano-convex lens and plano-concave lens is given by the magnification:

$$M = \frac{f_2}{f_1} = -5.25 \tag{C.2}$$

The magnification is negative, since the focal length associated with a plano-concave lenses is negative. The smallest focal length of plano-concave lens that is available in the catalogue is -24.0 mm (Thorlabs part # LC1975-C). A plano-convex lens with a focal length of 125.0 mm was chosen (Thorlabs part # LA1986-C), resulting in a magnification of 5.2-fold. To minimize spherical abberation, the CVI Melles Griot Technical Guide [9] was followed where the plano-concave lens was placed in reverse orientation and the plano-convex lens is in normal orientation. The ray diagram and lenses are shown in Fig. C.1. The expanded beam leaving the plano-convex lens is then directed into the objective lens and focused to a single point.

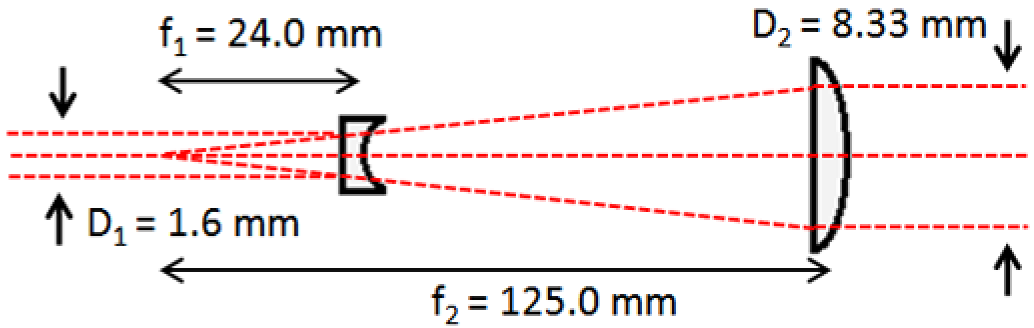

Figure C.1: Ray diagram of Galilean beam expander used for 5.2X expansion of a collimated beam.

A long-pass filter placed at a 45^o angle is used to allow light from the fiber collimator to pass into the objective lens. The filter reflects visible light, which allows for imaging of the sample to occur using a CCD tube that is placed perpendicular to the beam expander setup. The CCD tube contains the all of the focusing optics necessary to form an image on the CCD array. To collect the light on the other side of the sample, a convex lens with a large numerical aperture is used to focus the light onto an InGaAs photodetector. Fig. C.2 depicts the entire optical setup.

Focusing the laser spot onto a particular area of the sample requires that the user first determine where the spot is located on the CCD camera image. Using a photoluminescent card that absorbs IR light and emits green light, the spot is first located on the CCD with the card in focus. The card is then replaced with the sample and aligned so that the area of interest is centered where the spot was on the CCD.

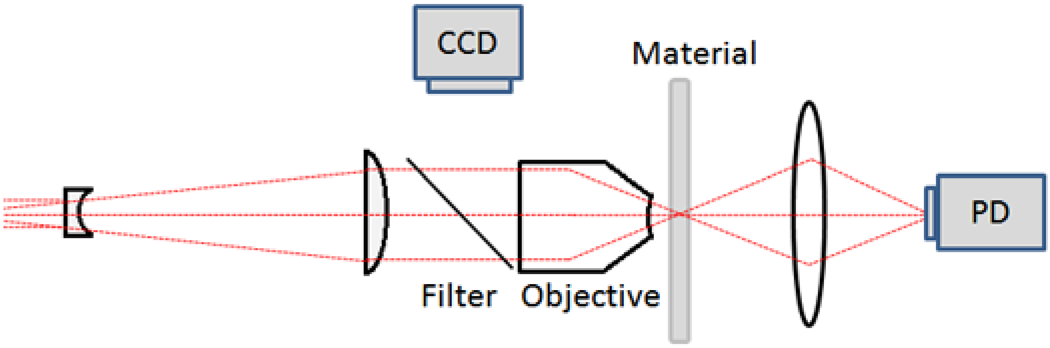

Figure C.2: Schematic of entire optical setup for measuring light transmission in bulk samples.